

The Impact of Plasma Dynamics on the Self-Magnetic-Pinch Diode Impedance

Nichelle Bennett¹, Dale R. Welch², Timothy J. Webb³, Michael G. Mazarakis³, Mark L. Kiefer³, M. Dale Crain¹, Darryl W. Droemer¹, Raymond E. Gignac¹, Mark D. Johnston³, Joshua J. Leckbee³, Isidro Molina¹, Dan Nielsen³, Robert Obregon¹, Tobias Romero³, Sean Simpson³, Chase C. Smith¹, Frank L. Wilkins¹, and Derek Ziska³

¹*National Security Technologies, LLC, Las Vegas, NV 89193*

²*Voss Scientific, LLC, Albuquerque, NM 87108 and*

³*Sandia National Laboratories, Albuquerque, NM 87185*

(Dated: March 3, 2015)

Abstract

The self-magnetic-pinch (SMP) diode is being developed as an intense electron beam source for pulsed-power-driven x-ray radiography. The basic operation of this diode has long been understood in the context of pinched diodes, including the dynamic effect that the diode impedance decreases during the pulse due to electrode plasma formation and expansion. Experiments being conducted at Sandia National Laboratories' RITS-6 accelerator are helping to characterize these plasmas using time-resolved and time-integrated camera systems in the x-ray and visible. These diagnostics are analyzed in conjunction with particle-in-cell simulations of anode plasma formation and evolution. The results confirm the long-standing theory of critical-current operation with the addition of a time-dependent anode-cathode gap length. The results may suggest that anomalous impedance collapse is driven by increased plasma radial drift, leading to larger-than-average ion $v_r \times B_\theta$ acceleration into the gap.

I. INTRODUCTION

The self-magnetic-pinch (SMP) diode [1–5] is being developed as an intense electron beam source for pulsed-power-driven x-ray radiography. The electron beam is generated via explosive field emission from the cathode [6] through a process of surface breakdown and formation of a cathode plasma. The beam subsequently deposits sufficient energy in the anode to cause thermal and stimulated desorption of surface contaminants, quickly breaking down and creating an anode plasma. Both plasmas are required for optimal beam generation and focus, but their dynamics can lead to a rapid collapse in the diode impedance and a degraded beam focus. In this paper, data from Sandia National Laboratories’ RITS-6 accelerator [7–9] are analyzed in conjunction with particle-in-cell (PIC) simulations in order to increase understanding of the operation of the SMP diode and its failure modes. Time-resolved diagnostics record the plasma motion and focal spot size [10–12], and simulations using hybrid PIC techniques [13] help interpret these measurements.

The basic operation of the SMP diode has long been understood in the context of pinched diodes [14, 15], including the dynamic effect in which the diode impedance decreases during the pulse due to electrode plasma expansion [16–19]. For example, the impedance is observed to decrease $\sim 0.33 \text{ } \Omega/\text{ns}$ during a nominal shot on RITS-6. (The nominal values for cathode diameter (d_c) and anode-cathode (AK) gap length (g) increase with voltage, as seen in Refs. 18 and 19, while maintaining $d_c \sim g$.) In addition, a more rapid impedance drop ($> 0.5 \text{ } \Omega/\text{ns}$ on RITS-6) occurs intermittently for otherwise nominal dimensions [20], and more frequently when nominal operational boundaries are exceeded. Both the nominal impedance lifetime and anomalous rapid impedance collapse are explored in this paper.

Reference 18 discusses the characteristics of intermittent SMP diode impedance collapse on RITS-6. For shots with identical diode geometries and pulsed power, a physical process sometimes occurs that causes a sharp rise in the diode current mid-pulse such that the diode suddenly carries nearly the total current in the transmission line. The source of this process was determined to be unrelated to the pulsed power, sheath electron current in the transmission line, or accelerator hardware. In this paper, sources within the diode are investigated. Diode hardware misalignment is ruled out as the sole contributor (see Sec. III) and shot-to-shot variations in expanding electrode plasmas remain [17] the prominent source.

The SMP diode’s design, theory, and operation are reviewed in Sec. II. Measurements

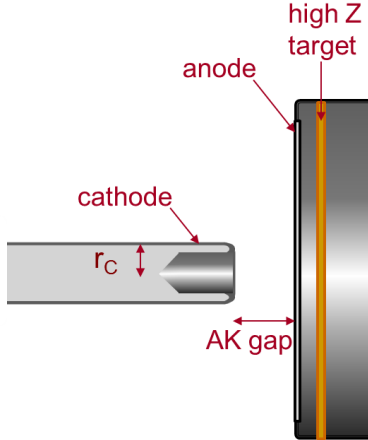


FIG. 1. Cross-sectional diagram of the SMP diode. Conductors are shown in gray. The surrounding volume is vacuum. For the nominal configuration $g \sim 2r_c$.

of the impedance lifetime and comparisons to the theory are also presented. These results motivate the plasma measurements and supporting simulations discussed in Secs. III and IV. Plasma dynamics are related to the beam focus and the normal impedance lifetime in Sec. IV. A possible mechanism for rapid impedance collapse is also discussed.

II. OPERATION OF THE SMP DIODE

The SMP diode is composed of a thin cylindrical cathode with a hollow, rounded tip, as illustrated in Fig. 1. In the results presented here, the final 2 mm of the cathode tip is coated with a silver paint to lower the emission threshold, encouraging rapid and uniform electron emission, as described in Reference 21. The anode is typically a planar foil in front of a high-atomic-number bremsstrahlung converter, with a diameter much larger than the cathode. Under an applied voltage pulse, an electron beam is emitted from the cathode and pinches as it approaches the anode due to its self-magnetic force. The pinch is limited by the beam's repulsive self-electric force (until transverse electric fields are canceled at the anode). As the beam heats the anode, contaminants are desorbed and ionized, rapidly forming a surface plasma. A space-charge-limited (SCL) ion current is drawn from this plasma and counterstreams with the electron beam. The ions partially charge-neutralize the beam, enabling a tighter pinch.

The theoretical diode current is calculated from the magnetic field at which electrons are

just cutoff from the anode by their Larmor radius. This critical condition [22] yields the current [3]

$$I_{crit} = 8.5\alpha \frac{r_c}{g} (\gamma^2 - 1)^{1/2} \quad [\text{kA}], \quad (1)$$

where r_c is the cathode radius and $\gamma = 1 + eV/m_e c^2$. α is a scale factor which has recently been shown to account for increased current from ion space-charge and deviations from Eq. 1 at small g/r_c [5].

Reference 18 demonstrated that an expanding anode plasma advects the anode potential, resulting in an effective g . Writing this as $g(t) = g_0 - v_p t$, where g_0 is the initial gap length and v_p is the combined anode and cathode plasma expansion velocity, Eq. 1 becomes [20]

$$I_{crit}(t) = 8.5\alpha \frac{r_c}{g_0 - v_p t} (\gamma^2 - 1)^{1/2} \quad [\text{kA}], \quad (2)$$

for constant γ .

We make two comparisons of measured diode current to critical current theory, which demonstrate the theory's validity. In the first, shown in Fig. 2, the average diode current is plotted as a function of aspect ratio (g_0/d_c) at five values of beam energy. The currents are recorded just as peak voltage is reached, at which time $g(t) \approx g_0$ (i.e., Eq. 1). These values show the same g_0/r_c scaling as I_{crit} , which is plotted at five corresponding values of γ using $\alpha = 2$. This value of α is consistent with Ref. 5. The second comparison plots the time-dependent currents for four shots against Eq. 2 using the measured $g(t)$. These comparisons are discussed in Sec. III B.

A collapsing diode impedance is observed upstream as a decrease in load impedance below what is expected for the diode and parallel free-electron current load. The SMP diode as fielded on RITS-6 is under-matched to the magnetically-insulated transmission line (MITL), so some sheath current is retrapped in the cathode for emission in the diode. The amount of retrapping is larger when the diode fails. Figure 3 illustrates this with a comparison of data from two shots, one with the nominal diode impedance lifetime (Shot 1581) and one with a collapsed impedance at the end of the pulse (Shot 1582). The transmission line currents (anode and cathode) are plotted in Fig. 3a. The voltage calculated from the anode and cathode currents [23, 24] is shown in Fig. 3b. The rise in the cathode current in the second half of the pulse marks the arrival of the retrapping wave. The diode current for Shot 1581, shown in Fig. 3c, represents the normal impedance decrease as shown in Fig. 3d. The diode impedance is estimated using the diode current and the upstream MITL voltage. The diode

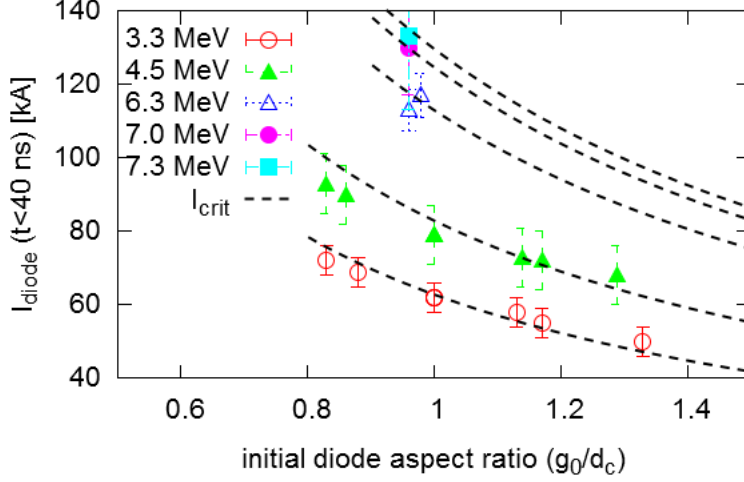


FIG. 2. Measured diode currents as a function of aspect ratio (g_0/d_c) for five beam energies. The currents are determined at the end of the pulse rise. I_{crit} from Eq. 1 is also plotted at each beam energy.

current for Shot 1582 increases above the normal range at approximately 70 ns. This current increase produces the more rapid decrease in impedance in Fig. 3d and the higher retrapped cathode current in Fig. 3a. The effect of the impedance drop on the radiation output is also shown in Fig. 3d. The forward-going radiation pulse is recorded using a Si PIN diode, which is sensitive to the low energy tail. The radiation pulse from Shot 1582 is shorter and correlated with a drop in the diode impedance.

Shot 1582 shares a characteristic of diode impedance collapse which is seen in a large number of shots from Ref. 18. Namely, these shots have the nominal diode current for some portion of the pulse and then an abrupt rise. These shots do not fail immediately and have a geometry which does not fail on average. The diagnostics and modeling effort described in the next section increase our understanding of this behavior.

III. ELECTRODE PLASMA MEASUREMENT

The diagnostics fielded on RITS-6 include current probes (such as plotted in Fig. 3), PIN diodes, optical imaging, and x-ray imaging systems. The current and PIN signals identify the impedance lifetimes. Two x-ray imaging systems provide information about the beam dynamics by measuring the time-integrated 2D beam focal spot size and the time-resolved

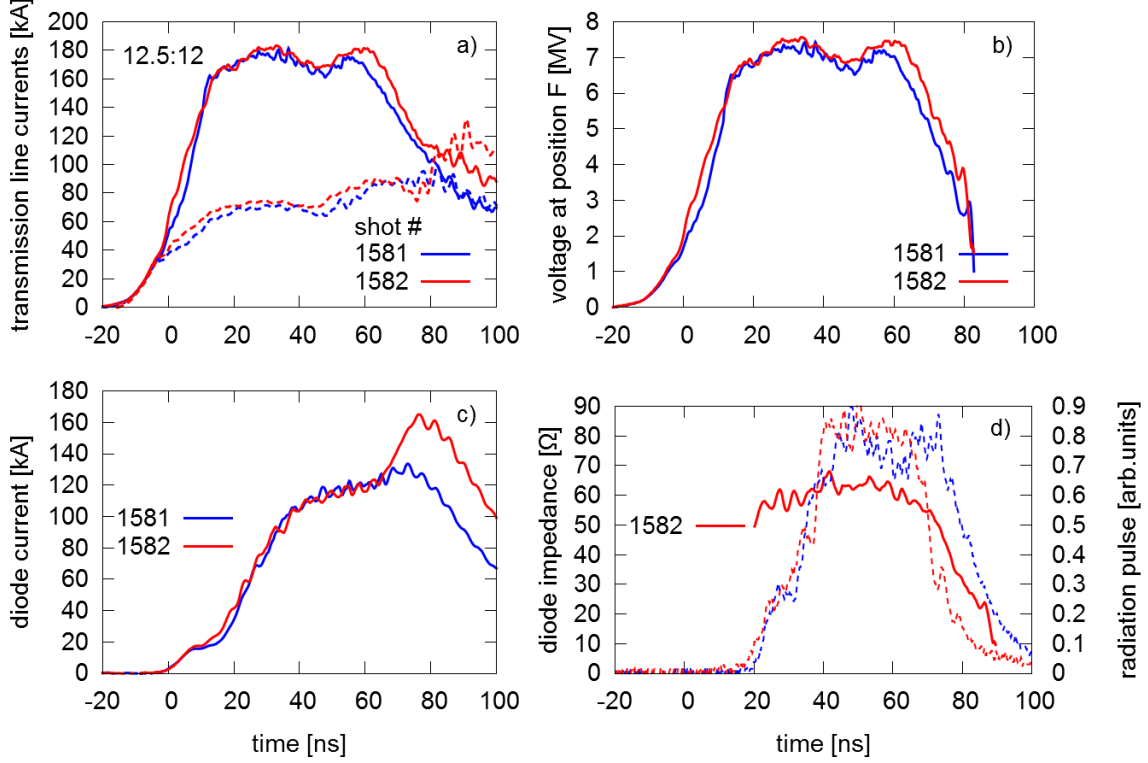


FIG. 3. Traces of the currents, voltage, diode impedance, and radiation pulse for two SMP diode shots with $d_c : g = 12.5:12$ mm. Shot 1581 (blue) shows nominal diode behavior while Shot 1582 (red) has a premature radiation pulse termination due to a rapid drop in diode impedance. The transmission line cathode (dashed) and anode (solid) currents are shown in a). The transmission line voltage is shown in b). The diode current is shown in c). The diode impedance (solid) and radiation pulse (dashed) are shown in d).

spot size [11, 12]. Two imaging systems in the visible spectrum are fielded to study electrode plasmas [10].

The plasma modeling techniques used to study the SMP diode preceded the optical diagnostics [13, 18], and simulations were originally only benchmarked against the diode current. In this paper we also compare the simulations to the x-ray spot size and plasma expansion images to estimate the typical level of surface contaminants on the anode foil. The details of the optical diagnostics are provided in Sec. III A. The simulation parameters that determine plasma evolution are chosen to achieve the best agreement with all available diagnostic results (Sec. IV.)

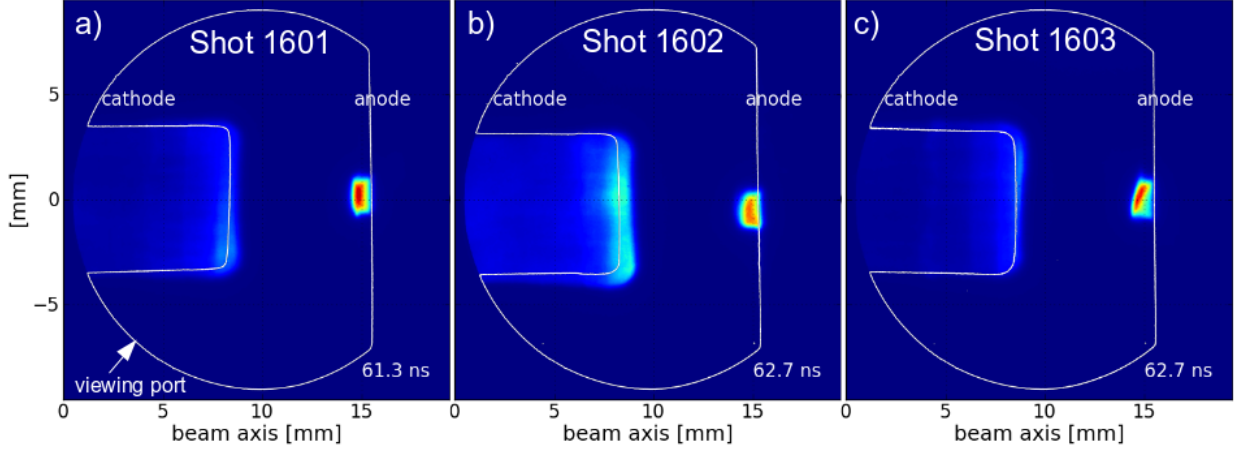


FIG. 4. Single-frame camera images for Shots 1601, 1602, and 1603 show shot-to-shot variation in the brightness of the electrode plasmas. A pre-shot image is converted to a contour plot of the diode hardware and viewing port, as shown in white. The cylindrical cathode is at left in each frame while the anode extends in the plane at right. The images have a 10-ns exposure beginning at the time listed at the bottom right in each frame. Times are relative to the rise in diode current.

A. Plasma imaging

The two optical diagnostic systems fielded on RITS-6 are oriented at 90° to the beam axis and image the continuum radiation from the electrode plasmas. The first, a single-frame camera, provides a 2D view of the cathode tip and anode surface centered on the AK gap and covering approximately 2 cm^2 with $126\text{-}\mu\text{m}$ resolution. The imaging is performed using a Princeton Instruments PI-MAX ICCD camera which features a front-illuminated CCD. Example images are shown in Fig. 4. The diode hardware is imaged prior to each shot and then converted to a contour plot outlining the electrodes and the viewing port of the vacuum chamber. These contours are then overlaid on each shot image to illustrate the extent of the plasma from the original surfaces.

The single-frame images consistently show a high-density region on the anode surface centered on axis and a cathode plasma extending $\sim 2 \text{ mm}$ upstream from the tip, independent of the cathode preparation. The cathode emission always exhibits a closely packed filamentary structure in azimuth, which is most evident in images taken between 18 and 35 ns. The filaments are similar to the structure observed for the paraxial diode cathode in

Reference 21. The anode plasma expands into the AK gap throughout the pulse.

There is more top-bottom asymmetry in the plasmas in some framing images than others, but this is not correlated with the intermittent impedance collapse. Quantifying the asymmetry as the difference in summed light intensities between the top and bottom of the anode or cathode in the images ($[\Sigma_{top} - \Sigma_{bottom}]/\Sigma_{total}$, where Σ is summed pixel intensities), the shots with more rapid impedance collapse have similar distributions for the anode and cathode as the nominal shots. The reduced $\chi^2 = 1/(N - 1) \sum_k^N [(\bar{x} - x_k)/\sigma]^2 = 1.26$ for the anode surface and $\chi^2 = 2.90$ for the cathode. Of the shots in Fig. 4, 1601 and 1603 exhibited normal impedance behavior while 1602 had a more rapid impedance collapse.

Other subtle differences may exist in the framing camera images for shots with collapsing impedance, such as differences in the spatial extent of the luminous plasma, but this is better analyzed with the second optical diagnostic, a streak-camera system. This diagnostic generates a time-resolved image of the plasma continuum along one axis. A photocathode converts the incident visible light to electrons which are then swept across a phosphor screen. The output visible light is recorded on a Princeton Instruments Quad-Ro CCD camera. The slit aperture for the incident light is oriented along the center of the AK gap axis, extending from the end of the cathode to the anode. During the pulse, the aperture image is swept across a camera CCD array. The example image in Fig. 5a shows the AK gap along the vertical axis and time along the horizontal. The timing of both the framing and streak camera diagnostics are calibrated such that $t = 0$ corresponds to I_{diode} reaching 1 kA.

The streak images typically show more plasma expanding from the anode than the cathode. The distance between the luminous plasma regions on the anode and cathode is calculated at each time interval ($0.24 \mu\text{s}/\text{pixel}$ on the camera CCD array) to give $g(t)$. The distance between the luminous plasma boundaries and the middle of the gap is calculated and then a time derivative is taken to yield the anode and cathode plasma velocities.

The average velocities of the luminous plasma boundaries (during peak power, 40–80 ns) are plotted in Fig. 6 as functions of AK gap length for four diode voltages. The average velocities are separated into distributions for nominal shots and for shots that experienced impedance collapse. The average measured anode plasma velocity under nominal impedance performance is $v_p = 3.3 \pm 0.3 \text{ cm}/\mu\text{s}$ and increases to $4.0 \pm 0.5 \text{ cm}/\mu\text{s}$ for shots with more rapid impedance collapse. The average measured cathode plasma velocity is $v_p = 2.6 \pm 0.4 \text{ cm}/\mu\text{s}$ and increases to $3.4 \pm 0.6 \text{ cm}/\mu\text{s}$ for shots with rapid impedance collapse. (The velocity for

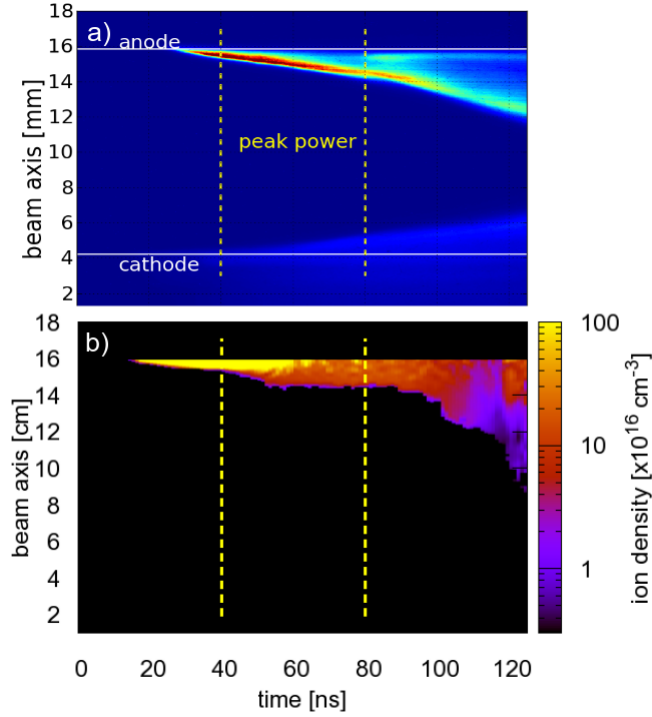


FIG. 5. a) Streak camera image for Shot 1581. The cathode is at the bottom and the anode is at the top. $t = 0$ is relative to the rise in diode current. Peak power occurs between the dashed lines. b) The time-dependent ion density distribution from simulation of Shot 1581 modeling only an anode plasma derived from a surface contaminant inventory of 700 monolayers at $r < 2$ mm and 10 monolayers elsewhere.

each shot is the average over 40 ns during peak power, even for shots in which the velocity appears to increase later in the pulse.) These results are in agreement with measurements by Etshessahar *et al.*, which yielded 3–5 cm/ μ s from the anode and 1–3 cm/ μ s from the cathode for a 12.5-mm cathode diameter [25]. They are also in agreement with the results of Cooper *et al.*, who measured a cathode plasma velocity of 3 cm/ μ s [21].

B. Time-dependent critical currents

The plasma diagnostics (along with the simulation results in Sec. IV) indicate that plasma expansion into the AK gap is sufficient to explain the nominal impedance lifetime of the SMP diode. The critical current in Eq. 2 accurately describes the data when $g(t) \approx g_0$ and $\alpha = 2$, as shown in Fig. 2. We also find that Eq. 2 is accurate for shots with collapsing diode

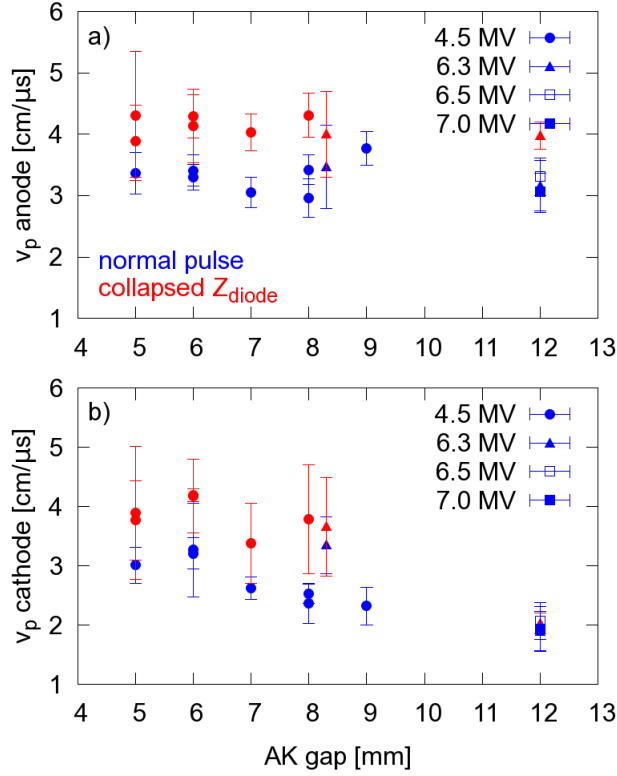


FIG. 6. Average velocities of the luminous plasma boundaries at peak diode electrical power on the a) anode and b) cathode plasma are plotted as functions of the AK gap length for four values of the diode voltage. The nominal shot averages are shown in blue and shots that experienced more rapid impedance collapse are shown in red.

impedance, for which $g(t)$ decreases more rapidly. To demonstrate, we calculate I_{crit} using the experimentally-determined $g(t)$ from the streak camera and compare it to the measured I_{diode} for a given shot. In this calculation of I_{crit} , we use $\alpha = 1.7$ to acknowledge that the luminous plasma region is smaller in extent than the plasma which advects the electrode potentials. Results for four shots, one nominal and three with more rapid impedance collapse, are plotted in Fig. 7. Figure 7b (shot 1582) is classified as rapid impedance collapse for this study because of the rapid increase in current at approximately 70 ns. This is more easily seen in the comparison of shots 1581 and 1582 in Fig. 3c. The estimated diode voltages, as input to γ , are also shown. The predicted and measured currents in Fig. 7 are in good agreement.

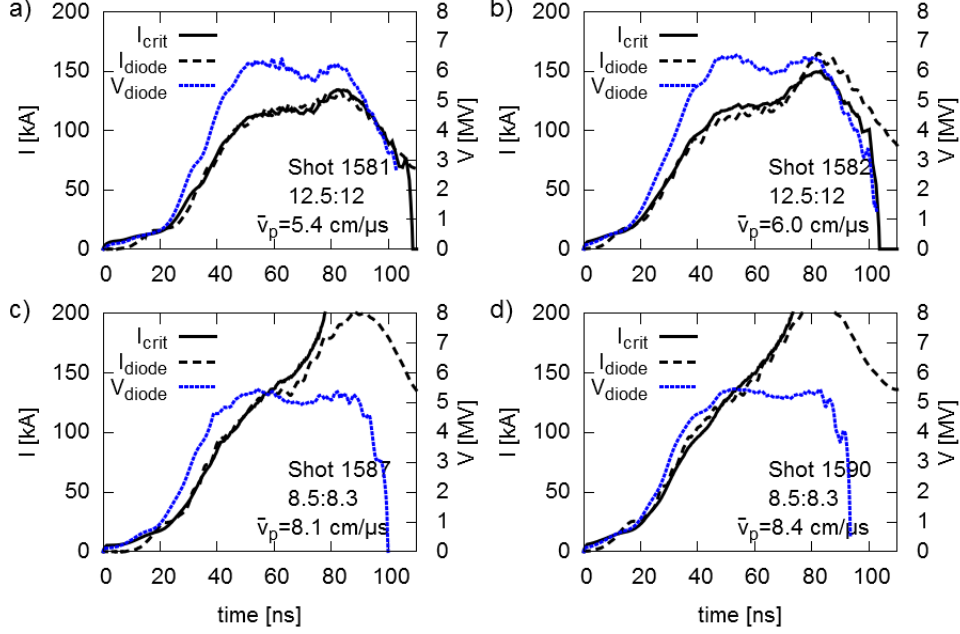


FIG. 7. Measured diode currents are plotted for four RITS-6 shots and compared to Eq. 2 using the measured $g(t)$ for each shot. The combined anode and cathode plasma velocities, averaged from 40 to 80 ns, are shown for each shot. The diode geometry in a) and b) is $d_c = 12.5$ and $g_0 = 12$ mm. The geometry in c) and d) is $d_c = 8.5$ and $g_0 = 8.3$ mm. V_{diode} is estimated from the transmission-line voltage and radiation pulse shape.

IV. ELECTRODE PLASMA SIMULATION

Simulations containing anode plasma formation and evolution have previously identified two mechanisms for falling impedance in the SMP diode [18]. We are now able to validate these mechanisms against the more extensive plasma diagnostics described in Sec. III. To do this, the measured voltage pulse for a specific shot is input as the simulation driving pulse. Examples of the measured voltage pulses are shown in Fig. 3b. Since modeling anode plasma formation and evolution is computationally intensive, only simulations conducted in 2D cylindrical coordinates are used in direct comparisons to data. A 3D Cartesian simulation is performed to investigate azimuthal asymmetries and 3D instabilities, however the plasma model is replaced by a Child-Langmuir model of thermal emission of protons from the anode surface to create bipolar flow.

Simulations are performed using the fully-relativistic electromagnetic particle-in-cell code LSP (version 12.4) [26]. The spatial extent covers 1.5 cm of the tip of the cathode needle

and the AK gap, with $80\text{ }\mu\text{m}$ -resolution in 2D and $120\text{ }\mu\text{m}$ in 3D. The 3D and 2D simulation geometries are illustrated in Fig. 8. Electron emission from the cathode is not currently modeled with a plasma, but as explosive emission after the local electric field stress exceeds the tolerance of the conductor [6, 27]. We use an emission threshold of 150 kV/cm , but note that the currents are insensitive to this choice given the fast pulse rise of the high applied voltages.

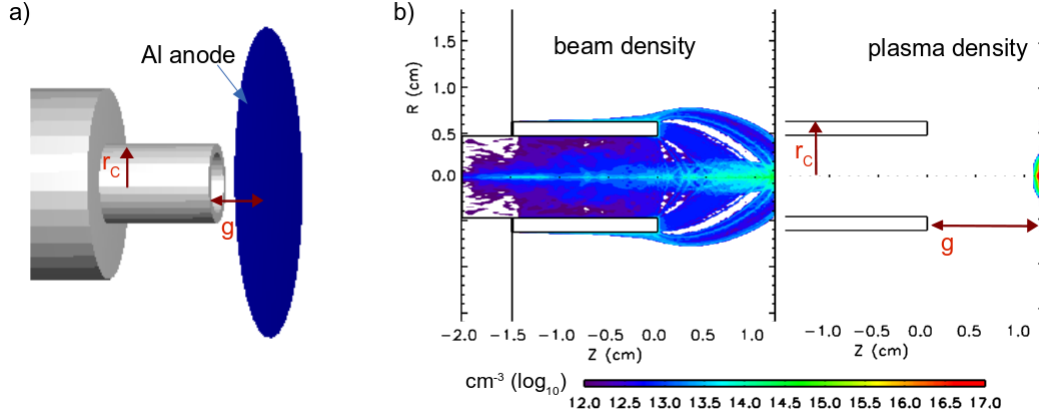


FIG. 8. a) The 3D Cartesian simulation geometry of the SMP diode. b) The 2D cylindrical (r, z) simulation geometry showing density contours for the electron beam and anode surface plasma at peak power (44 ns).

To model the anode plasma, a single neutral particle species is desorbed from the anode surface and fragmented into electron-ion pairs, as in Ref. 18. The surface density of adsorbed contaminant particles (n) decreases due to thermal and stimulated desorption at a rate given by [17, 28]

$$\frac{dn(t)}{dt} = -\nu_{th}n(t) e^{-Q_a/(RT(t))} - \frac{J_e\sigma n(t)}{e}, \quad (3)$$

where n is in units of monolayers or ML ($1\text{ ML} \equiv 10^{15}\text{ particles/cm}^2$), $\nu_{th} \sim 10^{13}\text{ s}^{-1}$, Q_a is the binding energy ($\sim 14 - 23\text{ kcal/mol}$ or $0.6 - 1\text{ eV}$), $R = 1.9858 \times 10^{-3}\text{ kcal/mol/K}$, T is the local surface temperature, J_e is incident electron current density, and σ is the stimulated desorption cross section ($\sim 1.25 \times 10^{-19}\text{ cm}^2$ [29–31]). The temperature increase ($T(t)$) is calculated from the energy deposited per particle path length (dE/dx) by the impacting electrons with charge q via $\Delta T = dE/dx q / (e\rho N_{av} C_p \cos \theta)$, where ρ is the material density, N_{av} is Avogadro's number, C_p is the material specific heat, and θ is the electron angle of incidence.

Experiments have shown that under 2×10^{-5} -Torr vacuum, a rough electrode surface can accrue over 45 monolayers of contaminants in 24 hours after cleaning [32]. With this magnitude as a guide, contamination levels are adjusted in simulation to achieve the best overall match to the measured diode current, single-frame image, streak-camera image, and time-resolved spot size.

To match to the measured diode impedance and currents, there must be sufficient desorption to supply the ion current with enough residual plasma to expand and create a steady decline in impedance. Simulations show that the ion current is 5–15% of the total current, depending on the ion mass [18]. The desorption rate required to support this current depends on the emission area, but is near 0.1 ML/ns, depending on emission radius, as shown in Fig. 9a. The thermal component of Eq. 3 quickly dominates at RITS current levels and Fig. 9b shows how quickly dn/dt rises with surface temperature. Figure 10 shows how quickly the anode surface heats in simulation. Shown is a contour map of temperature versus radius and time (for a particular choice of monolayers and binding energies). The dashed line indicates where $dn/dt > 0.1$ ML/ns, which provides a crude approximation to when the desorption exceeds what is required to sustain the bipolar flow, and thus when excess plasma would begin to expand from the surface.

The framing images (Fig. 4) show a very dense plasma region in the middle of the anode surface. Since significant anode material loss is observed post-shot, this dense region would be composed of foil atoms from a target material expansion, as well as contaminant species. However, a less dense plasma, below the framing camera sensitivity, must evolve concurrently over a wider region on the anode. If the plasma did not exist outside the imaged plasma region, there would not be the measured beam focus and gap closure. For example, a simulation without plasma but mimicking the conduction of the luminous plasma, i.e with a 2-mm-diameter conductor extending 1.5 mm from the anode surface centered on the beam axis, shows no change in diode impedance from a simulation without this extension. These images appear to corroborate the design choice of the hollow cathode made by previous investigators [1], since it may accommodate some on-axis anode material expansion.

The low-density anode plasma is expected to be composed of surface contaminants, which have long been identified as major contributors to electrode plasmas in vacuum-operated pulsed-power devices [16, 17]. The contaminants on an aluminum anode are expected to be dominated by C , H_2 , H_2O , CO , and CO_2 [16, 33], as well as oxide layers on the aluminum

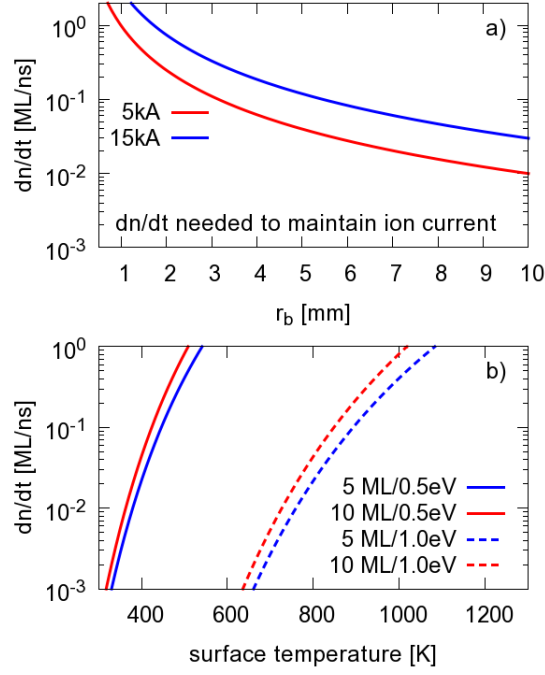


FIG. 9. a) The contaminant desorption rate dn/dt required to maintain a specified ion current as a function of desorption radius r_b . b) dn/dt from Eq. 3 plotted as a function of temperature assuming 5 and 10 monolayers with binding energies of 0.5 and 1.0 eV.

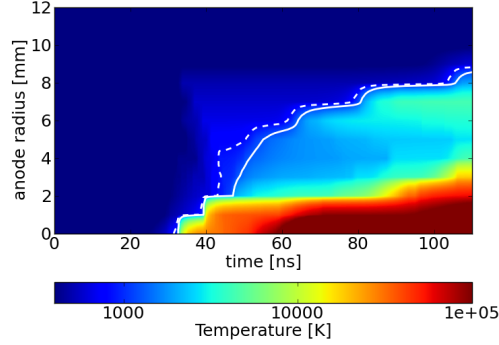


FIG. 10. The anode surface temperature as a function of radius and time from a 2D cylindrical simulation assuming a surface contaminant inventory of 700 ML at $r < 2$ mm and 10 ML elsewhere. The solid white line indicates where 75% of the surface contaminant inventory has desorbed. The dashed line indicates where $dn/dt > 0.1$ ML/ns.

foil.

The best match to the composite data set consisting of electrical, x-ray spot, and plasma expansion is achieved when the plasma model accommodates both contaminant desorption and target material expansion. Contaminant desorption is modeled over the region $r \geq 2$ mm using a 10 ML inventory with 1 eV binding energy. Target material expansion is approximated by assuming 700 ML in the region $0 \leq r < 2$ mm, also with 1 eV binding energy. Both regions use the C species to approximate all contaminants and target material in the desorbed plasma. The two regions create a high-density plasma ($\sim 10^{18} \text{ cm}^{-3}$) on axis which is not depleted during the pulse and a lower density plasma ($\sim 10^{15} \text{ cm}^{-3}$) which can advect the anode potential into the AK gap but may remain below camera thresholds. Figure 8b illustrates the extent of the resulting anode plasma from a 2D simulation. This can be compared to the framing images in Fig. 4.

The simulation results are not highly sensitive to these contaminant levels. Simulations using greater than 500 ML at $r < 2$ mm, and 10 to 15 ML elsewhere, still provide good comparisons to the framing images. However, when values below 500 ML at $r < 2$ mm are used in a simulation, the plasma erodes on axis such that it becomes less dense than the surrounding region rather than remaining more dense. When a contaminant inventory greater than 20 ML is used, the diode impedance collapses rapidly immediately, similar to the profile in Fig. 7d. Conversely, simulations with 5 ML or less at $r \geq 2$ mm have a stable diode impedance, rather than the steady impedance decline observed in nominal shots.

In addition to modeling a realistic impedance lifetime, the two-region desorption configuration also results in a rapid beam pinch, as shown in comparisons to the time-resolved spot size and diode current in Fig. 11. The visible anode plasma expands into the AK gap with velocity $v_p = 3.1 \text{ cm}/\mu\text{s}$. Without the high desorption on axis, corresponding to the 700-ML contaminant inventory, the beam pinches more slowly which allows for greater anode heating at larger radius, with a temperature profile that is broader radially from the one in Fig. 10. For example, when a contaminant inventory of 10 ML is used over the entire anode surface, the beam requires an additional 1.5 ns to focus. Higher heating at larger radius results in more contaminant desorption over a larger region, such that the lower contaminant inventory actually causes a more rapid gap closure.

A crude synthetic streak-camera image of the anode plasma from the 2D simulation is shown in Fig. 5b. As with the comparison to the framing camera, this image is created from

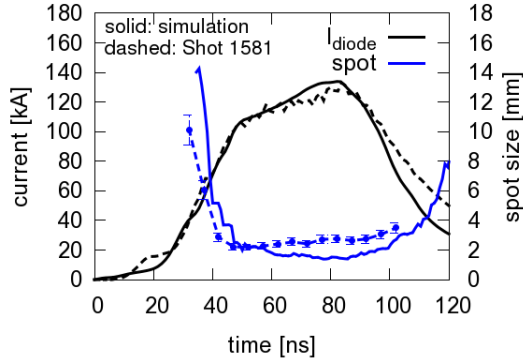


FIG. 11. The measured diode current and spot size from Shot 1581 are compared to results from a 2D cylindrical simulation which uses contaminant levels of 700 ML at $r < 2$ mm and 10 ML elsewhere.

the plasma density without accounting for plasma temperature or opacity. More realistic synthetic images could be achieved by tracking the plasma ionization state and radiative properties with an equation-of-state model. This is the focus of future work. A unified model of plasma creation on both electrodes is also under construction.

The beam focus remains stable in the 2D simulation, while in 3D with only counter-streaming protons, the beam radius at the target begins to increase immediately after the beam pinches. This is caused by a continuously growing beam emittance, seen in the snapshots plotted in Fig. 12. The emittance growth is driven by azimuthal filaments in the electron density at the cathode. These filaments are similar to those imaged by the framing camera.

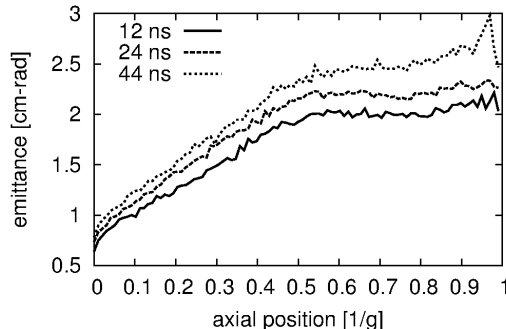


FIG. 12. Simulated electron beam emittance as a function of axial position normalized to the AK gap length, g , at 12, 24, and 44 ns. Results are from a 3D Cartesian simulation with surface emission of protons to create bipolar current.

In addition to spot size growth, 3D simulations also demonstrate spot drift along the target. Figure 13 shows the radial offset of the electron and proton beams at the anode as functions of time. The drift in Fig. 13 must be a result of a small $x - y$ displacement by either the electron or ion channels. A displacement in the ion channel exerts a force on the electron beam in the direction of the displacement. This increases ion emission from the anode at the new beam location which, in turn, causes the offset to grow. The displacement may be initiated by ion beam transverse (betatron) oscillations in the AK gap. The onset of oscillations coincides with the beam pinch around 10 ns into the pulse, when the ion current reaches it peak. The transverse oscillations in the dense on-axis plasma channel are shown in Fig. 14, where the wavelength is seen to be roughly half the AK gap length and the frequency is near 3 GHz. These betatron oscillations are not azimuthally symmetric, but pinch to a helix oriented along the z -axis, indicating a delayed pinch on one axis by $\sim 1/2\lambda_\beta$ with respect to the other.

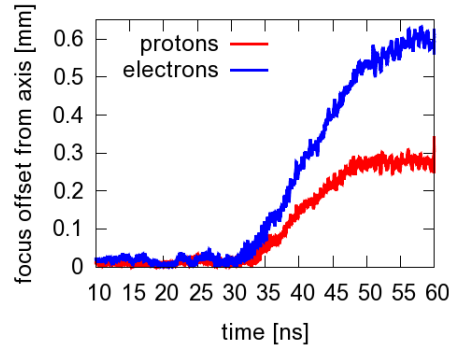


FIG. 13. Simulated radial offset from the original beam axis for the protons and electrons at the anode as functions of time. A 5-GHz low-pass filter is applied.

As discussed previously, high levels of contaminants cause an immediate rapid impedance collapse similar to Fig. 7d but do not explain the abrupt transition in impedance seen in Figs. 7b and 7c. Instead, a collapse of this type, although not as abrupt, is achieved in simulation with an intermediate level of contaminants (10 ML) and no representation of on-axis target material expansion, as shown in Fig. 15. In this case, anode heating is more uniform radially than in Fig. 10, creating a more radially uniform surface plasma density. The plasma is more readily depleted on-axis as the bipolar ion current is drawn from that region, and this leads to more significant radial drift in the plasma. While the azimuthal magnetic field profile in the plasmas is similar in all simulations, the larger ion positive

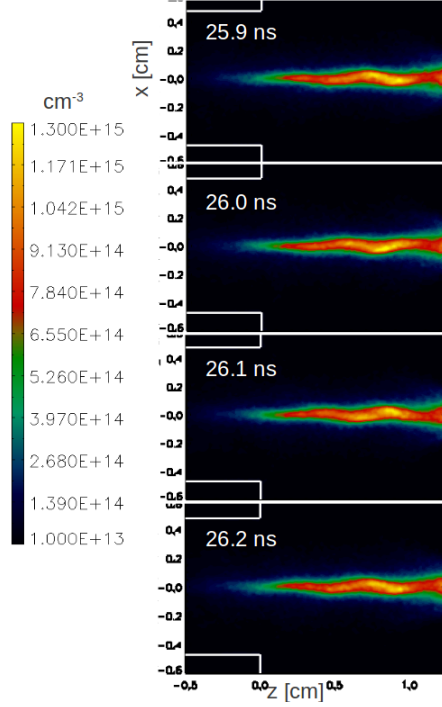


FIG. 14. Simulated electron density contours in the x, z plane during peak power exhibit oscillations.

radial velocity in this case results in larger $v_r \times B_\theta$ acceleration into the gap and as well as an increase in ion population surrounding the cathode. This, in turn, boot-strapped another current-increasing mechanism, increased emission along the cathode, as described in Ref. 18 and subsequently seen in streak-camera images. The I_{diode} for this simulation is compared to Shots 1581 and 1582 in Fig. 15. We speculate that the mechanism seen in simulation could be at play in Shots 1581 and 1582 as well since the diode currents for all three have the same profile for the first 65 ns.

While this result was artificially achieved by under populating the on-axis plasma, nonuniformities in the plasma could result in increased $v_r \times B_\theta$ acceleration. These nonuniformities could result from the electron-ion dynamics derived from the 3D simulation. As seen in Fig. 7, the smaller the original AK gap length, the faster the impact of plasma expansion on impedance. Although all four shots in Fig. 7 have $d_c/g_0 \sim 1$ which yields the same I_{crit} initially, the value of $g(t) = g_0 - v_p t$ decreases more rapidly for smaller g_0 .

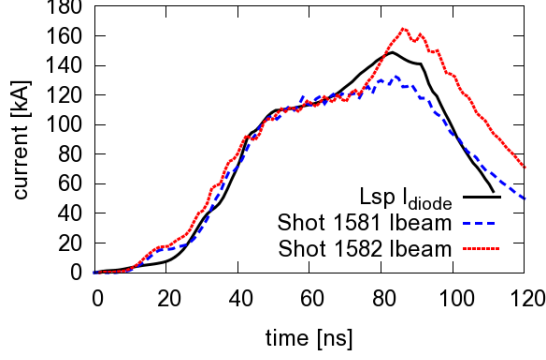


FIG. 15. Measured diode currents from Shots 1581 (normal impedance lifetime) and 1582 (rapid impedance collapse) are compared to a simulation with a uniform 10-ML surface contaminant inventory. In the simulation, the diode impedance collapses due to larger-than-average ion $v_r \times B_\theta$ acceleration.

V. CONCLUSION

Time-resolved and time-integrated camera systems in the x-ray and visible regions fielded on RITS-6 are providing a more detailed picture of the operation of the SMP diode. These measurements are supported by hybrid PIC simulations, which model the creation and evolution of anode plasmas. By simultaneously matching the measured luminous anode plasma spatial extent, time-dependent diode current, and time-dependent beam focal spot to simulation results, we are able to discriminate among anode surface contaminant levels and interpret plasma expansion velocities. The simulation which best matches data includes surface contaminants with an initial inventory at the 10-ML level and a larger target material expansion within the beam focal radius.

We have verified the original interpretation of the SMP diode as a current-limited device [3] with the addition of a time-dependent AK gap. The time-dependent gap, $g(t)$, is approximated from streak-camera images of luminous plasma, although simulations indicate that the plasma density responsible for advecting the anode potential into the gap is below the camera sensitivity. When this is accounted for by using a larger value for the I_{crit} scaling parameter α , the theoretical currents calculated with measured $g(t)$ agree well with measured currents for shots with nominal diode impedance and impedance collapse.

Simulations with the nominal impedance lifetime exhibit an anode plasma expansion velocity of $v_p = 3.1 \text{ cm}/\mu\text{s}$, which is close to the average measured value of $v_p = 3.3 \pm$

0.3 cm/ μ s. The average measured cathode plasma velocity for the nominal impedance lifetime is $v_p = 2.6 \pm 0.4$ cm/ μ s. Anomalous impedance collapse occurs in simulations when a plasma is desorbed more uniformly across the anode. In this case the plasma density is more readily depleted on-axis as the bipolar ion current is drawn from that region. This leads to more significant radial drift in the plasma and larger-than-average ion $v_r \times B_\theta$ acceleration into the gap. This, in turn, can boot-strap with other current-increasing mechanisms such as increased emission along the cathode needle. This mechanism for rapid impedance collapse is only speculative since the underlying physical process is unknown and it has not been verified in experiment.

Simulation results will be enhanced with the addition of a unified model of plasma creation. This model will enable the consistent creation of plasmas on both electrodes and incorporate both the contaminant evolution and target material expansion self-consistently. The inclusion of an equation-of-state formalism for tracking plasma ionization states and radiative properties will enable better comparisons of simulation results to the optical imaging diagnostics and to the spectroscopic system fielded on RITS [34]. An equation-of-state model will also be used in a quasi-neutral formalism to quantify the anode material heating and expansion. Of specific interest is the beam heating of the foil and converter, the heating of the foil from back-streaming converter material, and the ability of the foil to constrain this back-streaming material. Finally, measurements are underway to determine the typical contaminant inventories and species, and their variability.

VI. ACKNOWLEDGMENTS

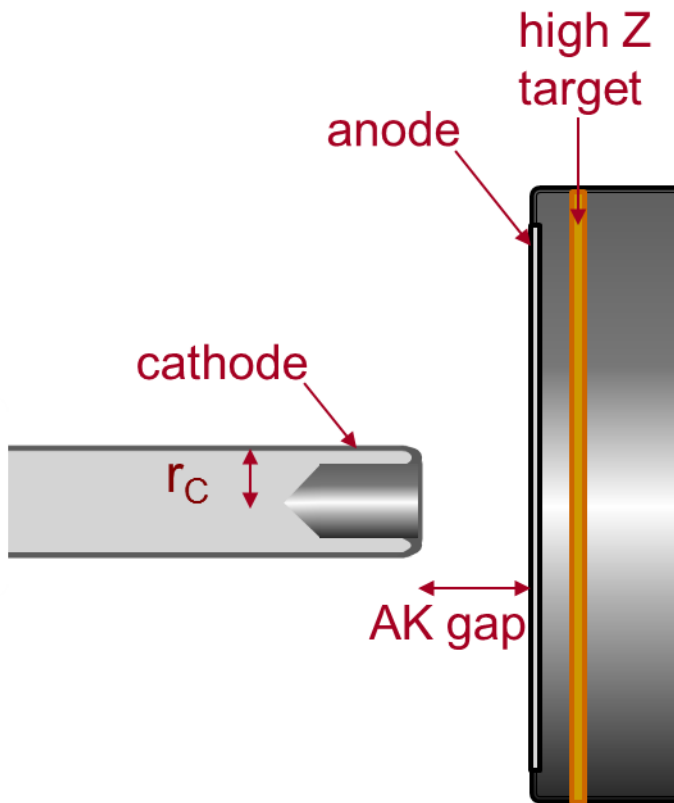
This manuscript has been authored by National Security Technologies, LLC, under Contract No. DE-AC52-06NA25946 with the U.S. Department of Energy. The United States Government retains and the publisher, by accepting the article for publication, acknowledges that the United States Government retains a non-exclusive, paid-up, irrevocable, world-wide license to publish or reproduce the published form of this manuscript, or allow others to do so, for United States Government purposes. The U.S. Department of Energy will provide public access to these results of federally sponsored research in accordance with the DOE Public Access Plan (<http://energy.gov/downloads/doe-public-access-plan>). This work was also supported by the Sandia National Laboratories, Sandia Corporation, a wholly owned

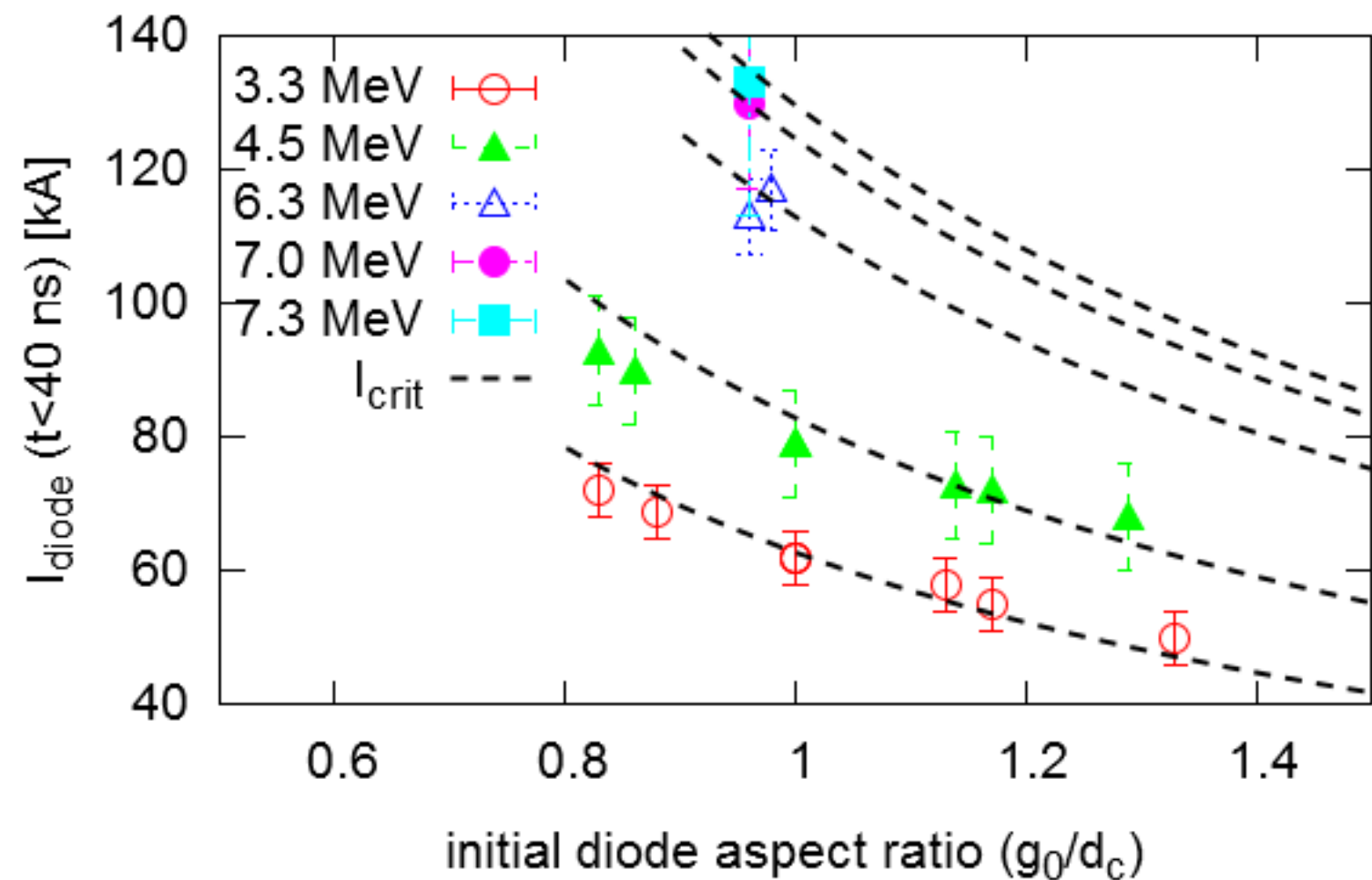
subsidiary of Lockheed Martin Company, for the U.S. Department of Energy's National Nuclear Security Administration under Contract DE-AC04-94AL85000.

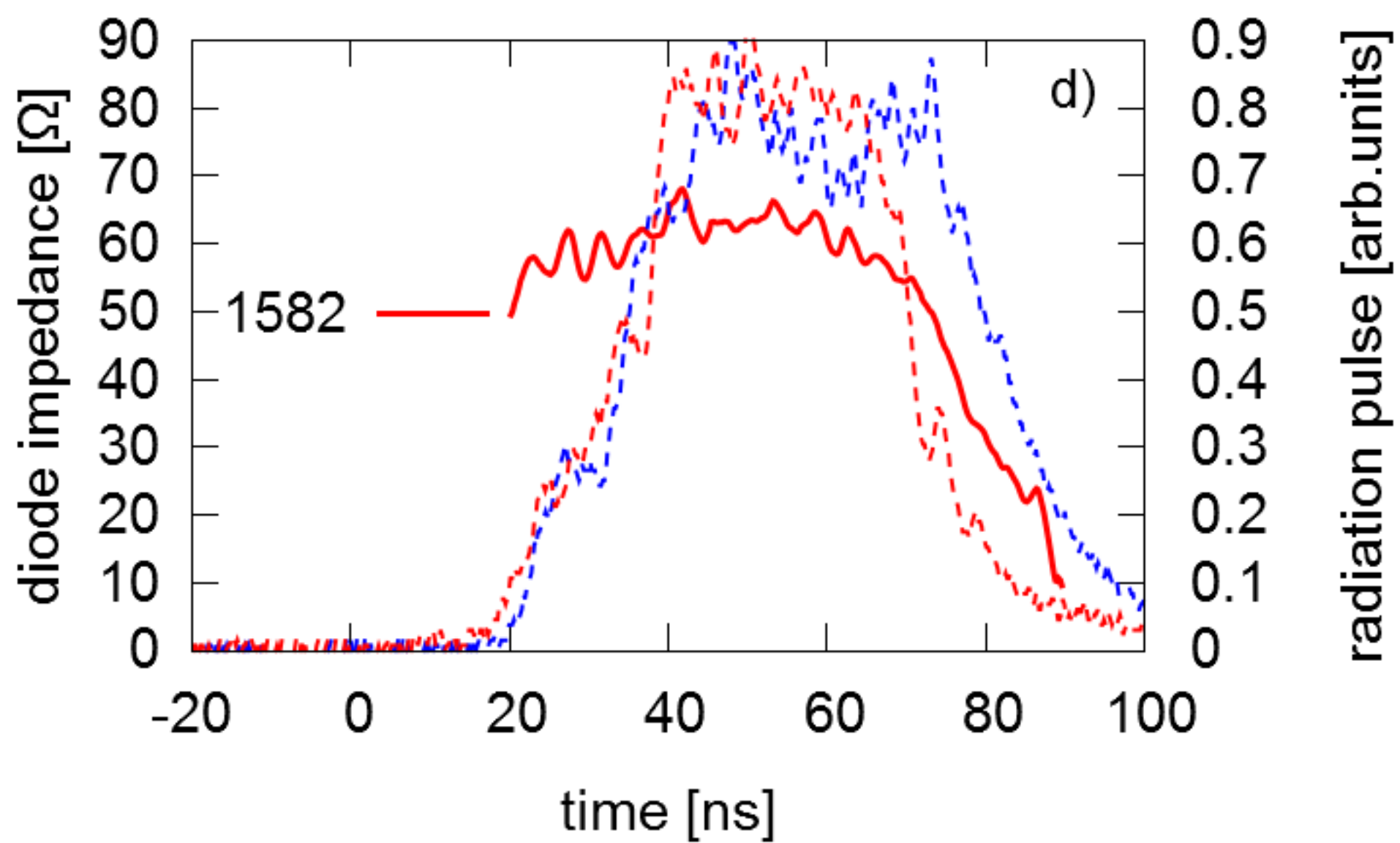
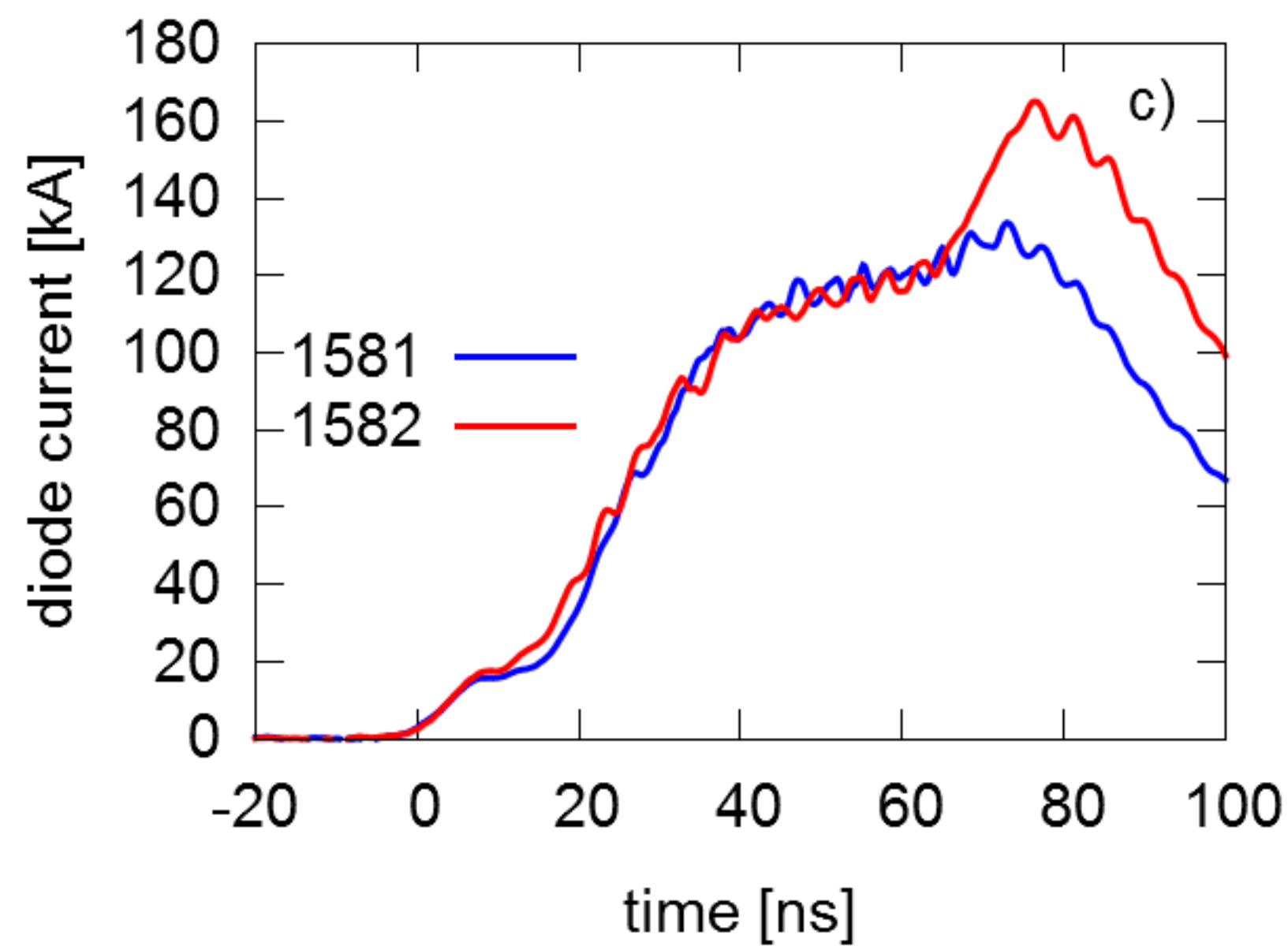
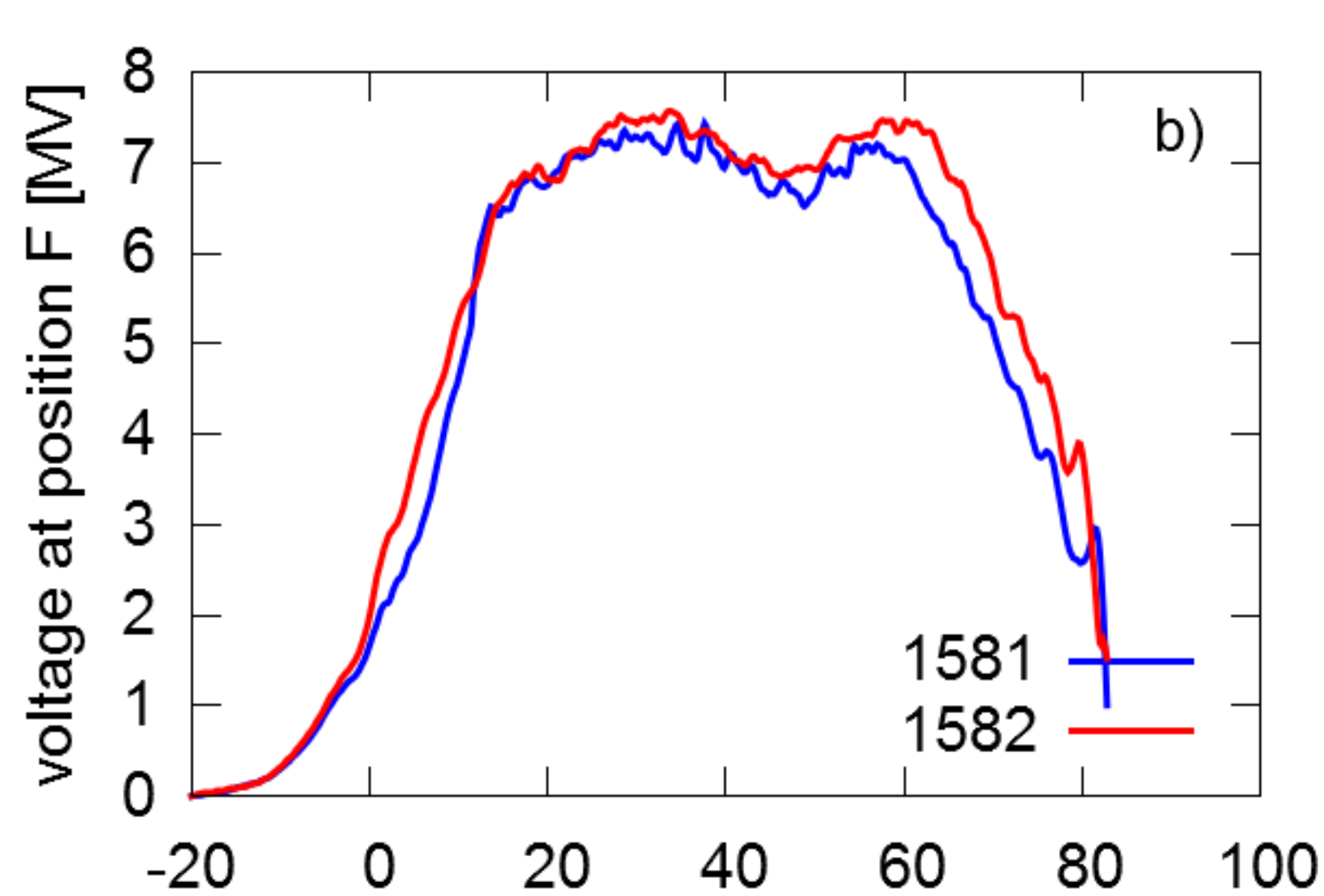
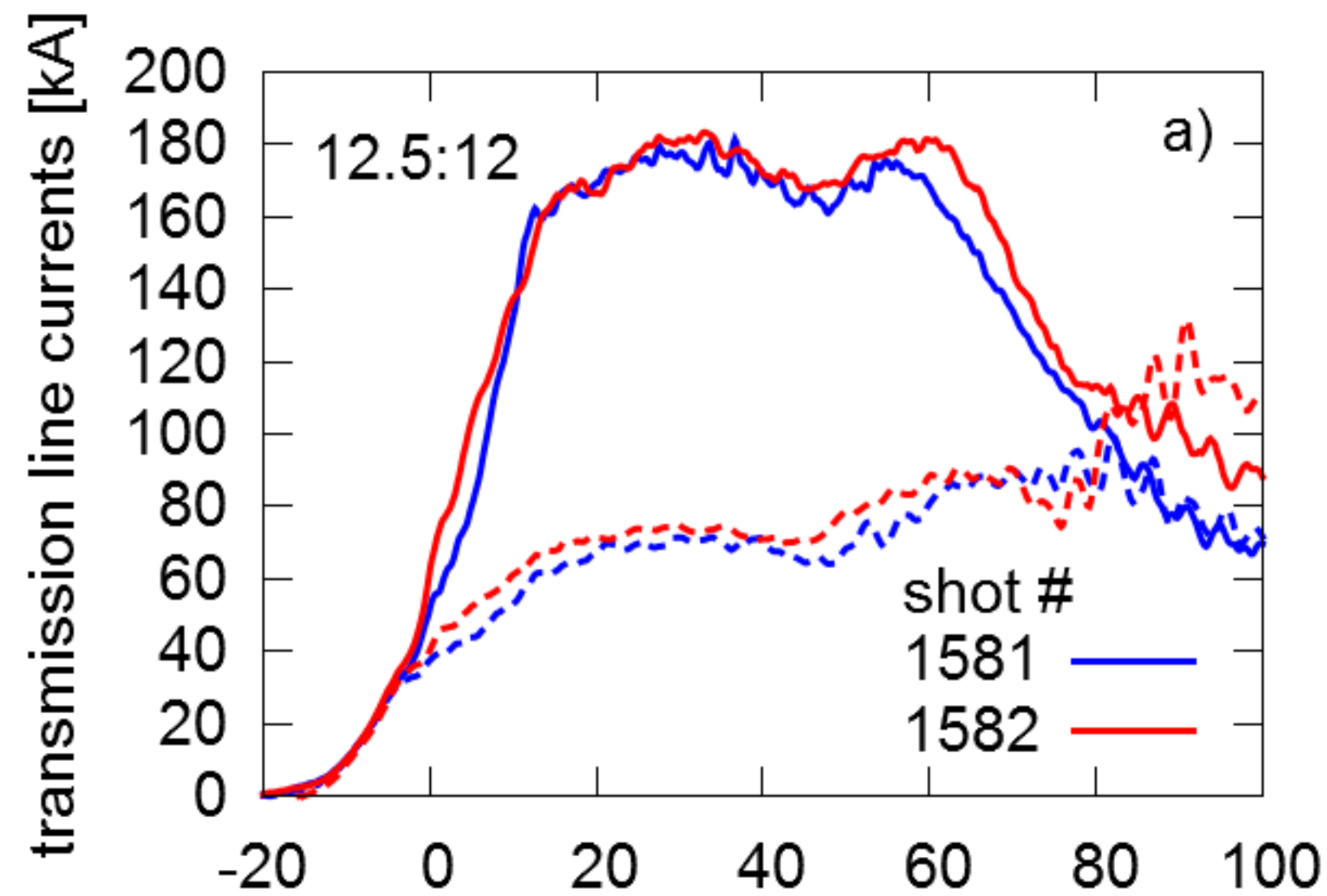
- [1] J. Threadgold, I. Crotch, D. Rose, and J. Maenchen, in *Proc. of the 14th IEEE International Pulsed Power Conference* (IEEE, 2003) p. 995.
- [2] K. D. Hahn, N. Bruner, S. Cordova, R. Gignac, M. D. Johnston, J. Lechbee, I. Molina, B. V. Oliver, S. Portillo, J. Threadgold, T. J. Webb, D. R. Welch, and D. Ziska, *IEEE Trans. Plasma Sci.* **38**, 2652 (2010).
- [3] S. Swanekamp, G. Cooperstein, J. Schumer, D. Mosher, F. Young, P.F.Ottinger, and R. Commisso, *IEEE Trans. Plasma Sci.* **32**, 2004 (2004).
- [4] D. Hinshelwood, G. Cooperstein, D. Mosher, D. Ponce, S. Strasburg, S. Swanekamp, S. Stephanakis, B. Weber, F. Young, A. Critchley, I. Crotch, and J. Threadgold, *IEEE Trans. Plasma Sci.* **33**, 696 (2005).
- [5] P. Martin, J. Threadgold, and S. Vickers, *IEEE Trans. Plasma Sci.* **41**, 2510 (2013).
- [6] R. Fowler and L. Nordheim, *Proc. Royal Society London, A* **119**, 173 (1928).
- [7] I. Smith, V. L. Bailey, J. Fockler, J. S. Gustwiller, D. L. Johnson, J. E. Maenchen, and D. W. Droemer, *IEEE Trans. Plasma Sci.* **28**, 1653 (2000).
- [8] D. Johnson, V. Bailey, R. Altes, P. Corcoran, I. Smith, S. Cordova, K. Hahn, J. Maenchen, I. Molina, S. Portillo, E. Puetz, M. Sceiford, D. V. de Valde, D. Rose, B. Oliver, D. Welch, and D. Droemer, in *Proc. of the 15th IEEE International Pulsed Power Conference* (IEEE, 2005) pp. 314–317.
- [9] N. Bruner, T. Genoni, E. Madrid, D. Rose, D. Welch, K. Hahn, J. Leckbee, S. Portillo, B. Oliver, V. Bailey, and D. Johnson, *Phys. Rev. ST Accel. Beams* **11**, 040401 (2008).
- [10] D. Droemer, M. Crain, G. Lare, N. Bennett, and M. Johnston, in *Proc. 19th IEEE Pulsed Power Conference* (2013) pp. 1–6.
- [11] S. Lutz, D. Droemer, D. Devore, D. Rovang, S. Portillo, and J. Maenchen, in *Proc. 14th IEEE Pulsed Power Conference*, Vol. 1 (2003) pp. 197–200 Vol.1.
- [12] S. Portillo, S. Lutz, L. P. Mix, K. Hahn, D. Rovang, J. E. Maenchen, I. Molina, S. Cordova, D. Droemer, R. Chavez, and D. Ziska, *IEEE Trans. Plasma Sci.* **34**, 1908 (2006).

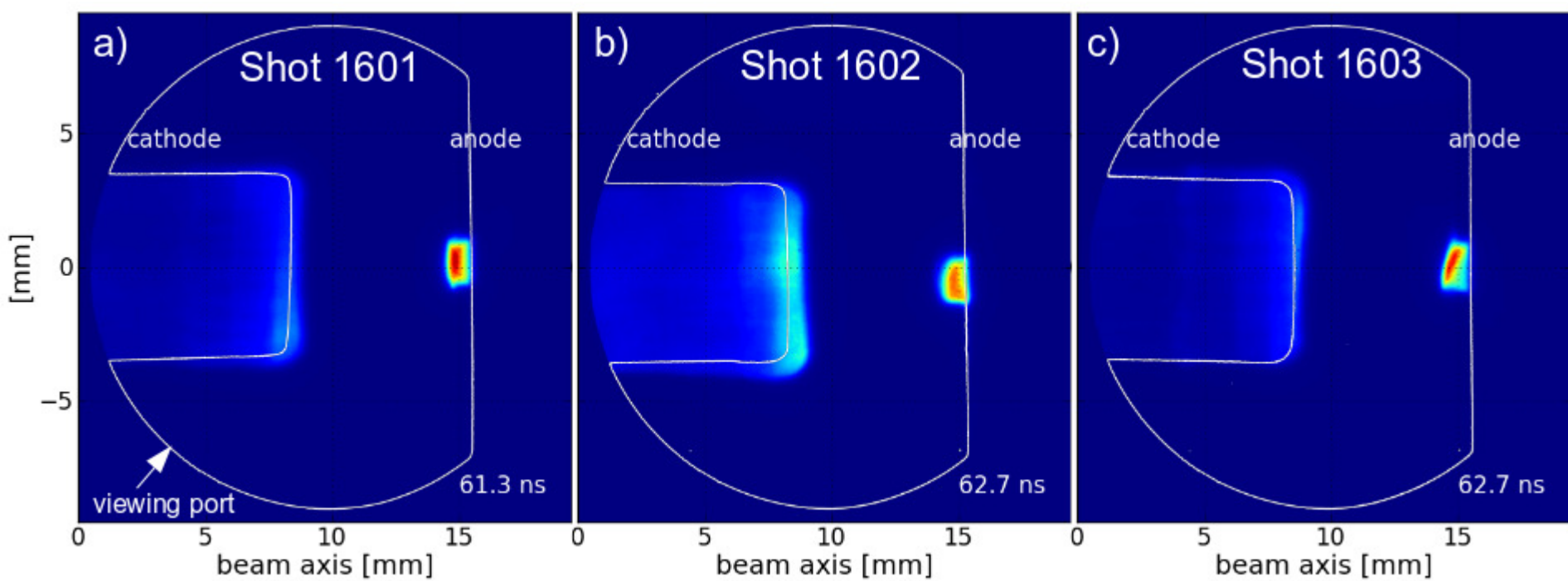
- [13] D. R. Welch, D. V. Rose, N. Bruner, R. E. Clark, B. V. Oliver, K. D. Hahn, and M. D. Johnston, *Phys. Plasmas* **16**, 123102 (2009).
- [14] S. B. Swanekamp, R. Commisso, G. Cooperstein, P. F. Ottinger, and J. W. Schumer, *Phys. Plasmas* **7**, 5214 (2000).
- [15] J. Maenchen, K. Hahn, M. Kincy, D. Kitterman, R. Lucero, P. Menge, I. Molina, C. Olson, D. Rovang, R. Fulton, R. Carlson, J. Smith, D. Martinson, D. Droemer, R. Gignac, T. Helvin, E. Ormand, F. Wilkins, D. Welch, B. Oliver, D. Rose, V. Bailey, P. Corcoran, D. Johnson, I. Smith, D. Weidenheimer, G. Cooperstein, R. Commisso, D. Mosher, S. Stephanakis, J. Schumer, S. Swanekamp, F. Young, T. Goldsack, G. Cooper, A. Pearce, M. Phillips, M. Sinclair, K. Thomas, M. Williamson, S. Cordova, R. Woodring, and E. Schamiloglu, in *BEAMS 2002: 14th International Conference on High-Power Particle Beams*, Vol. 650 (AIP Conference Proceedings, 2002) pp. 117–122.
- [16] D. Hinshelwood, *IEEE Trans. Plasma Sci.* **11**, 188 (1983).
- [17] M. E. Cuneo, P. R. Menge, D. Hanson, W. Fowler, M. Bernard, G. Ziska, A. Filuk, T. Pointon, R. Vesey, D. Welch, J. E. Bailey, M. Desjarlais, T. Lockner, T. Mehlhorn, S. Slutz, and M. Stark, *IEEE Trans. Plasma Sci.* **25**, 229 (1997).
- [18] N. Bruner, D. R. Welch, K. D. Hahn, and B. V. Oliver, *Phys. Rev. ST Accel. Beams* **14**, 024401 (2011).
- [19] P. N. Martin, J. R. Threadgold, A. Jones, J. McLean, G. M. Cooper, K. Webb, G. Jeffries, and P. Juniper, *IEEE Trans. Plasma Sci.* **39**, 1943 (2011).
- [20] N. Bennett, M. D. Crain, D. W. Droemer, R. E. Gignac, G. Lare, I. Molina, R. Obregon, C. C. Smith, F. L. Wilkins, D. R. Welch, S. Cordova, M. L. Gallegos, M. D. Johnston, M. L. Kiefer, J. J. Leckbee, M. G. Mazarakis, D. Nielsen, T. J. Renk, T. Romero, T. J. Webb, and D. Ziska, *Phys. Rev. ST Accel. Beams* **17**, 050401 (2014).
- [21] G. Cooper, J. McLean, P. Martin, R. Davitt, and K. Stuart, *IEEE Trans. Plasma Sci.* **36**, 1278 (2008).
- [22] J. M. Creedon, *J. Appl. Phys.* **48**, 1070 (1977).
- [23] J. M. Creedon, *J. Appl. Phys.* **46**, 2946 (1975).
- [24] C. W. Mendel, *J. Appl. Phys.* **50**, 3830 (1979).
- [25] B. Etchessahar, R. Maisonne, M. Toury, L. Hourdin, B. Bicrel, B. Cassany, T. Desanlis, L. Voisin, F. Cartier, S. Cartier, T. D’Almeida, C. Delbos, A. Garrigues, D. Plouhinec, S. Rit-

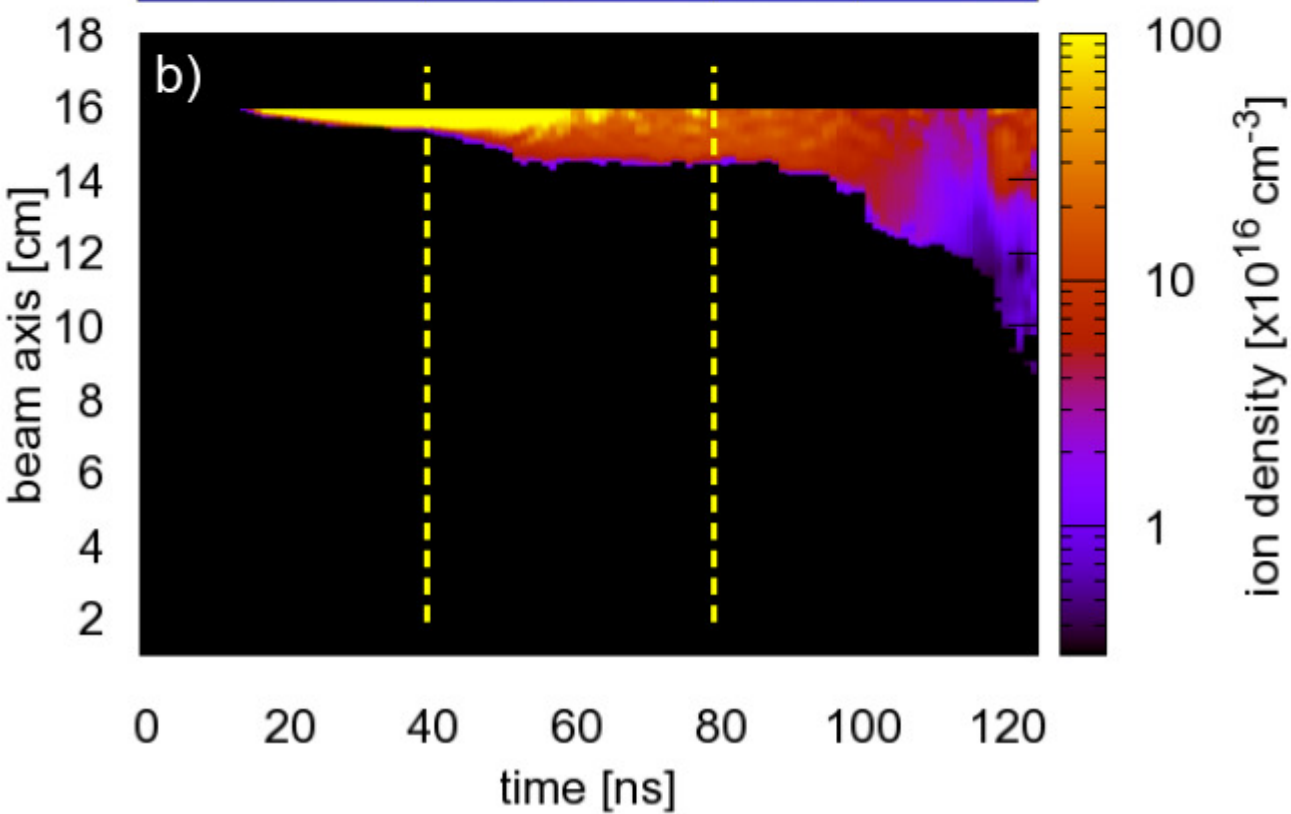
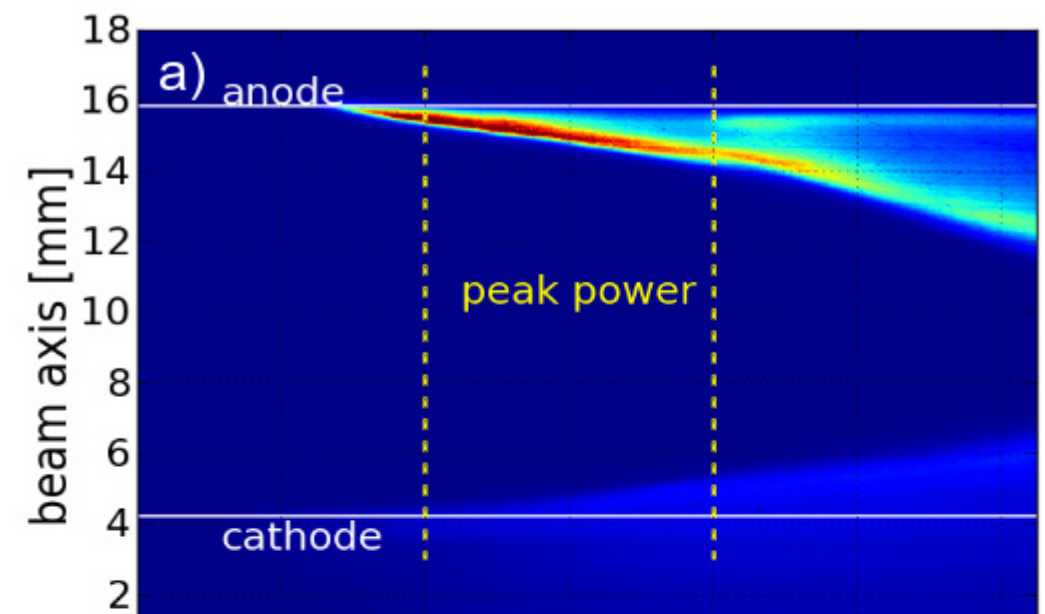
- ter, D. Sol, F. Zucchini, and M. Caron, *Physics of Plasmas* (1994-present) **20**, 103117 (2013).
- [26] D. Rose, D. R. Welch, B. V. Oliver, R. E. Clark, D. L. Johnson, J. E. Maenchen, P. R. Menge, C. L. Olson, and D. C. Rovang, *J. Appl. Phys.* **91**, 3328 (2002).
- [27] I. Langmuir and K. Blodgett, *Phys. Rev.* **22**, 347 (1923).
- [28] P. Redhead, *The Physical Basis for Ultrahigh Vacuum* (Chapman and Hall, London, 1968).
- [29] T. E. Madey and J. John T. Yates, *J. Vac. Sci. Technol.* **8**, 525 (1971).
- [30] S. W. Bellard and E. M. Williams, *Surface Science* **80**, 450 (1979).
- [31] D. R. Welch and T. P. Hughes, *Laser and Particle Beams* **16**, 285 (1998).
- [32] P. R. Menge and M. E. Cuneo, *IEEE Trans. Plasma Sci.* **25**, 252 (1997).
- [33] H. F. Dylla, *J. Vac. Sci. Technol. A* **6**, 1276 (1988).
- [34] M. D. Johnston, B. V. Oliver, S. Portillo, J. E. Maenchen, T. A. Mehlhorn, D. R. Welch, D. V. Rose, N. Bruner, D. Droemer, Y. Maron, and A. D. Heathcote, in *Proc. of the 34th IEEE International Conference on Plasma Science* (IEEE, 2007) p. 445.

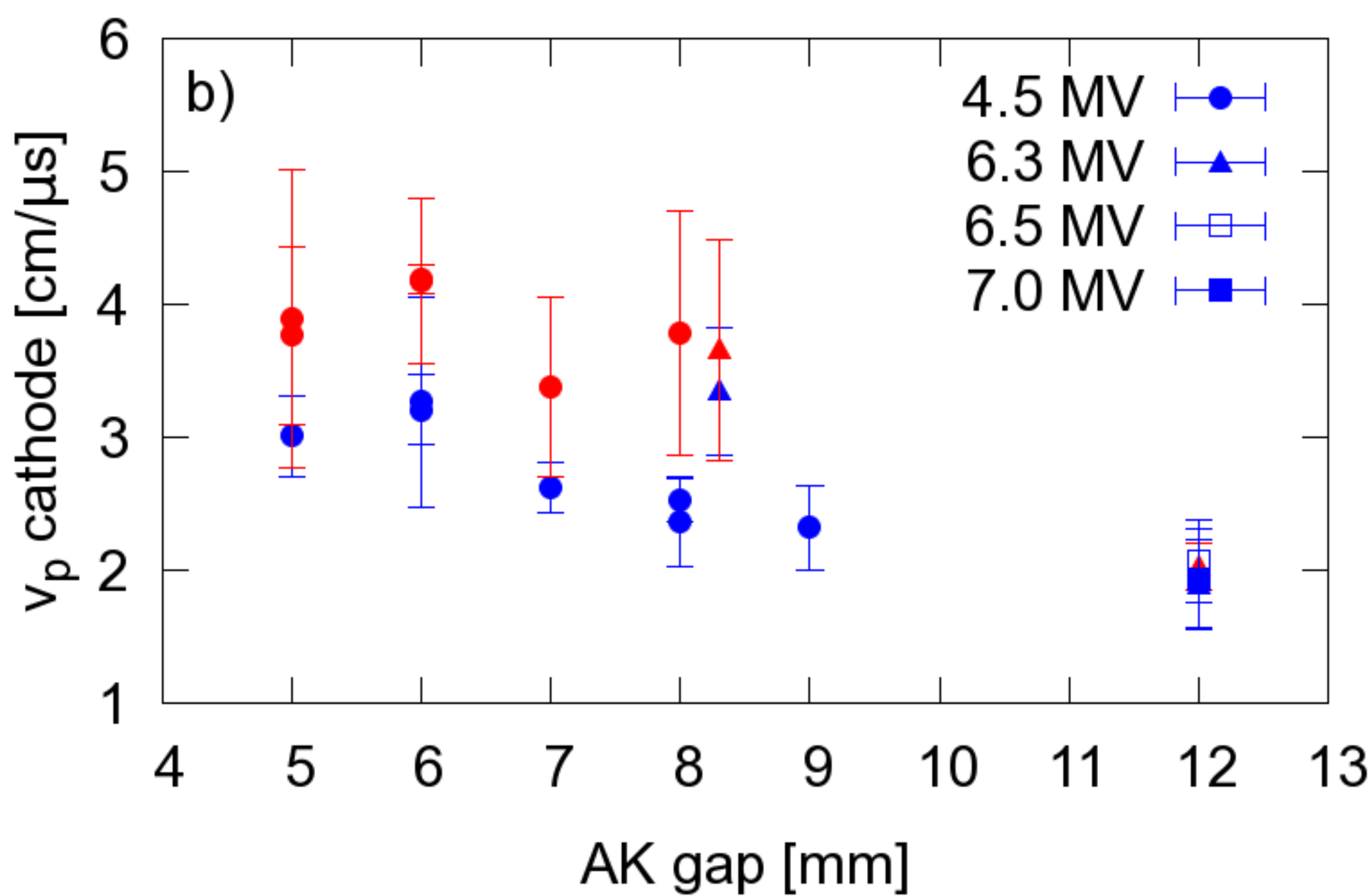
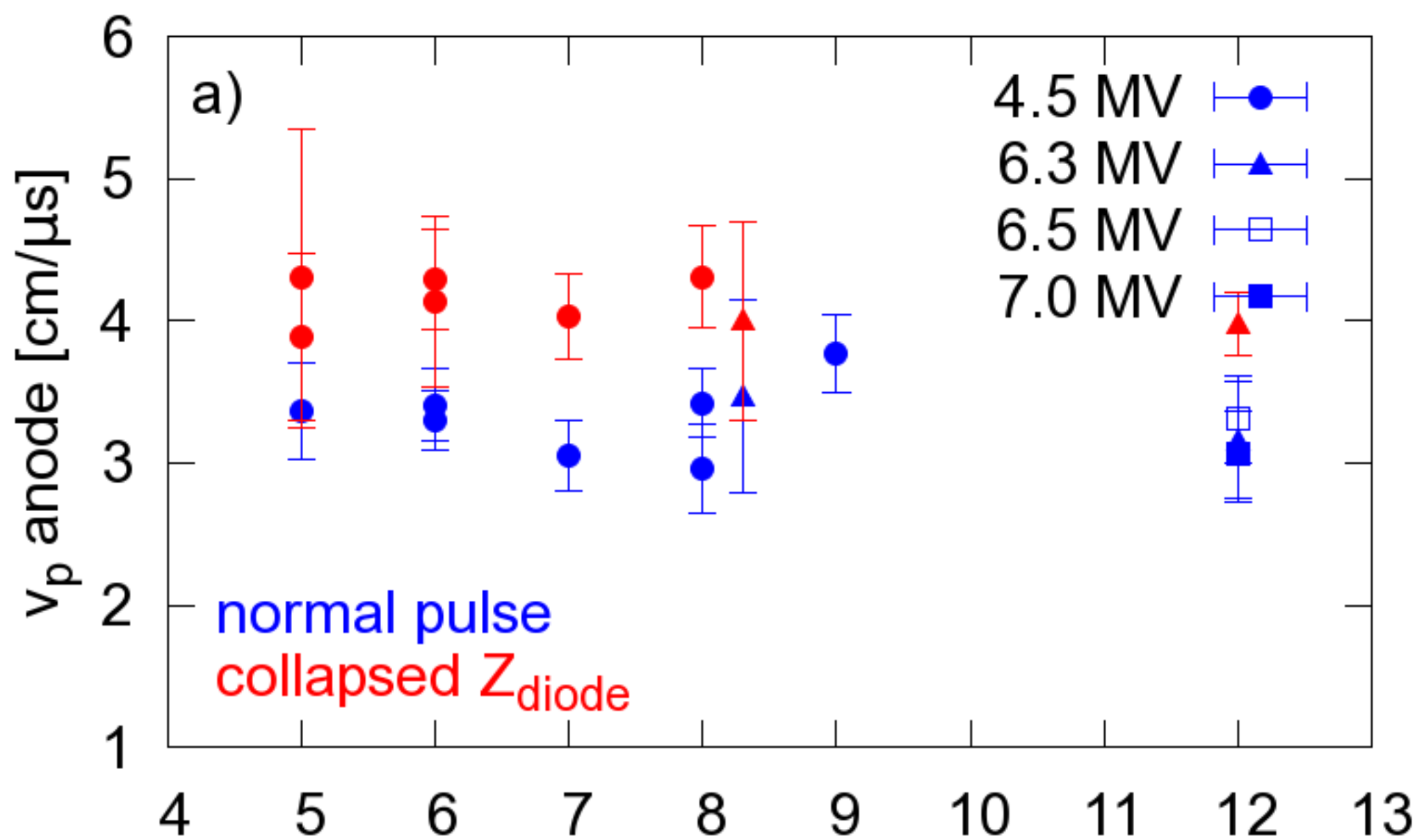


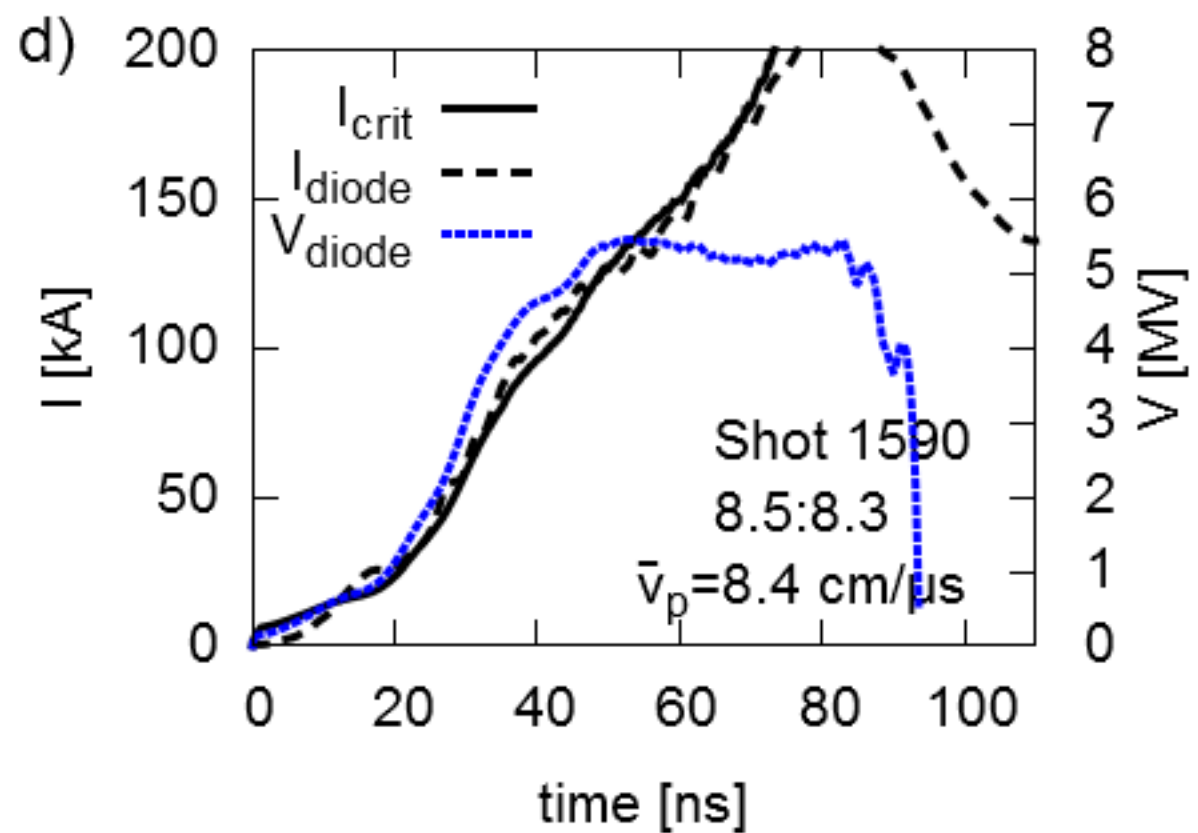
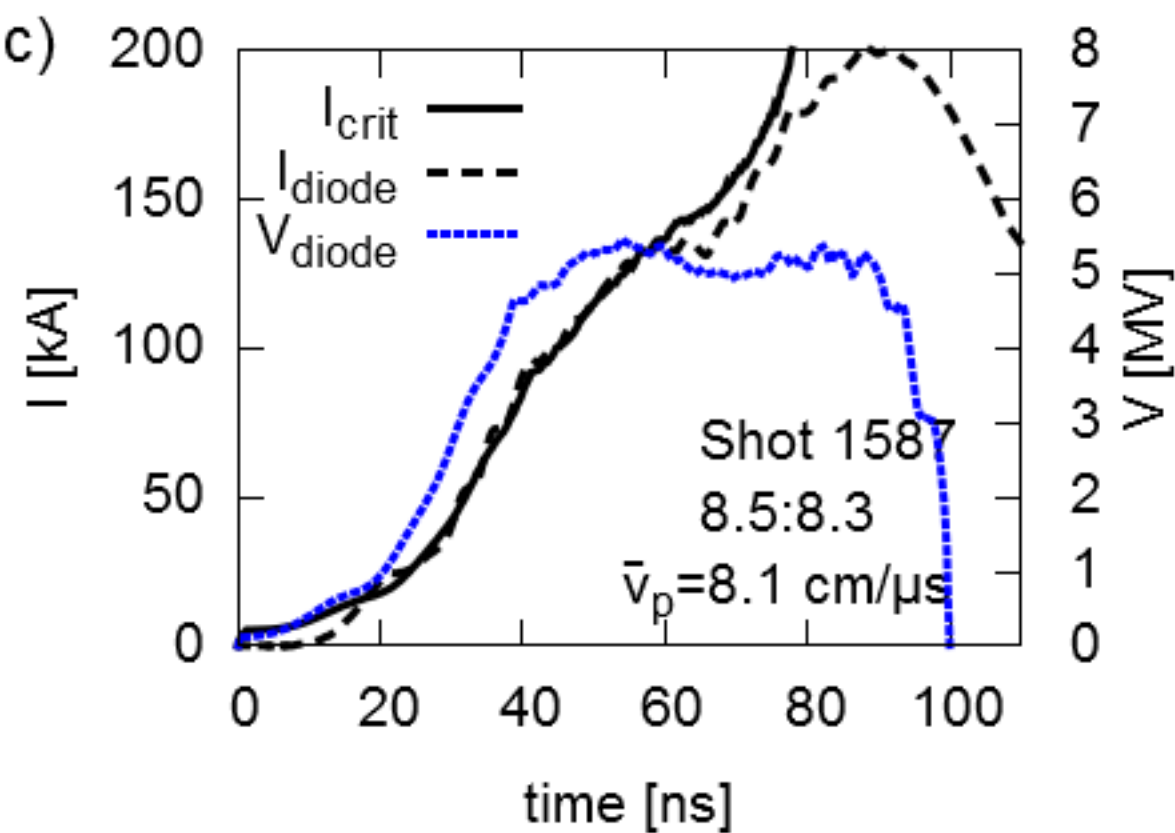
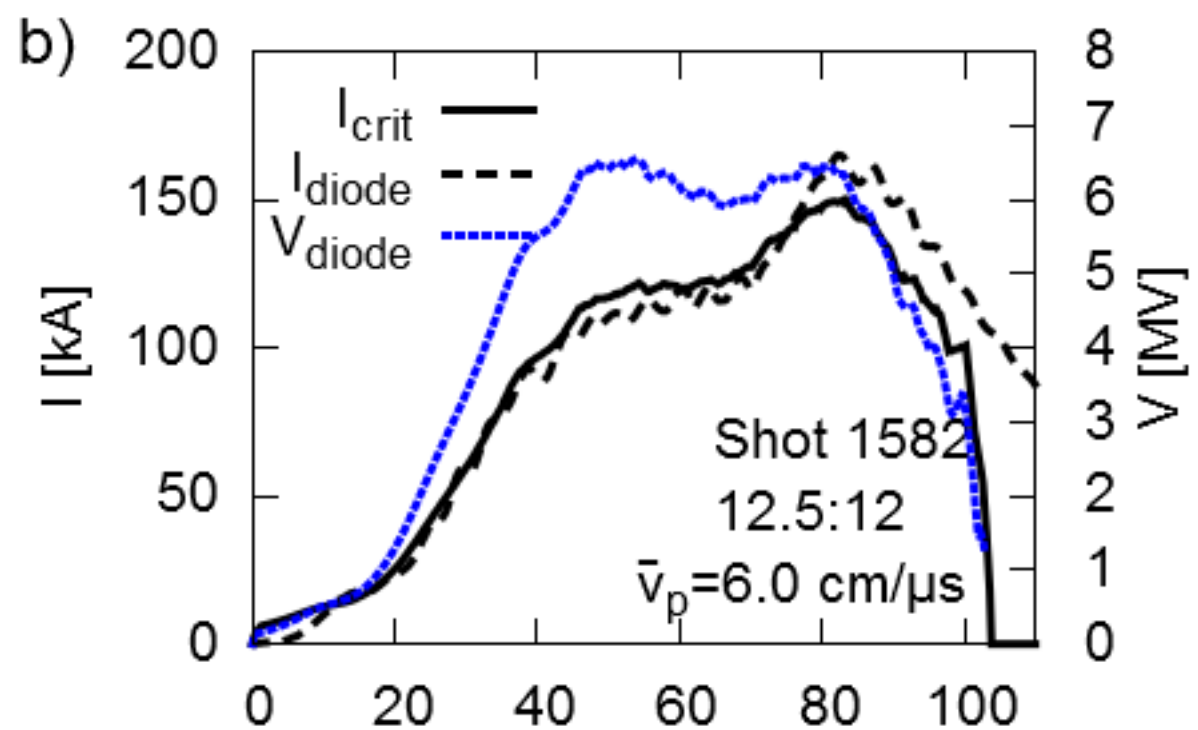
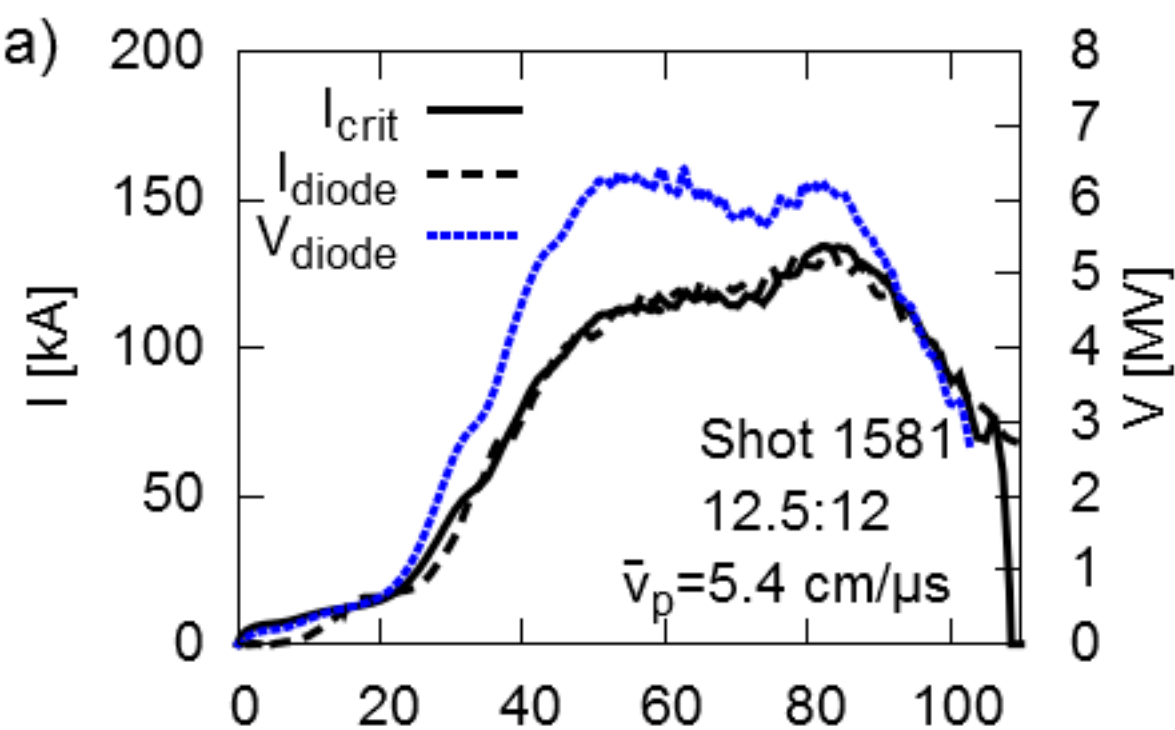




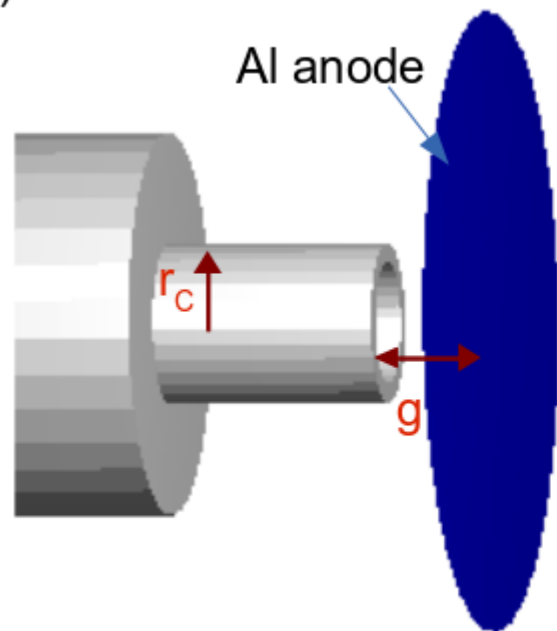




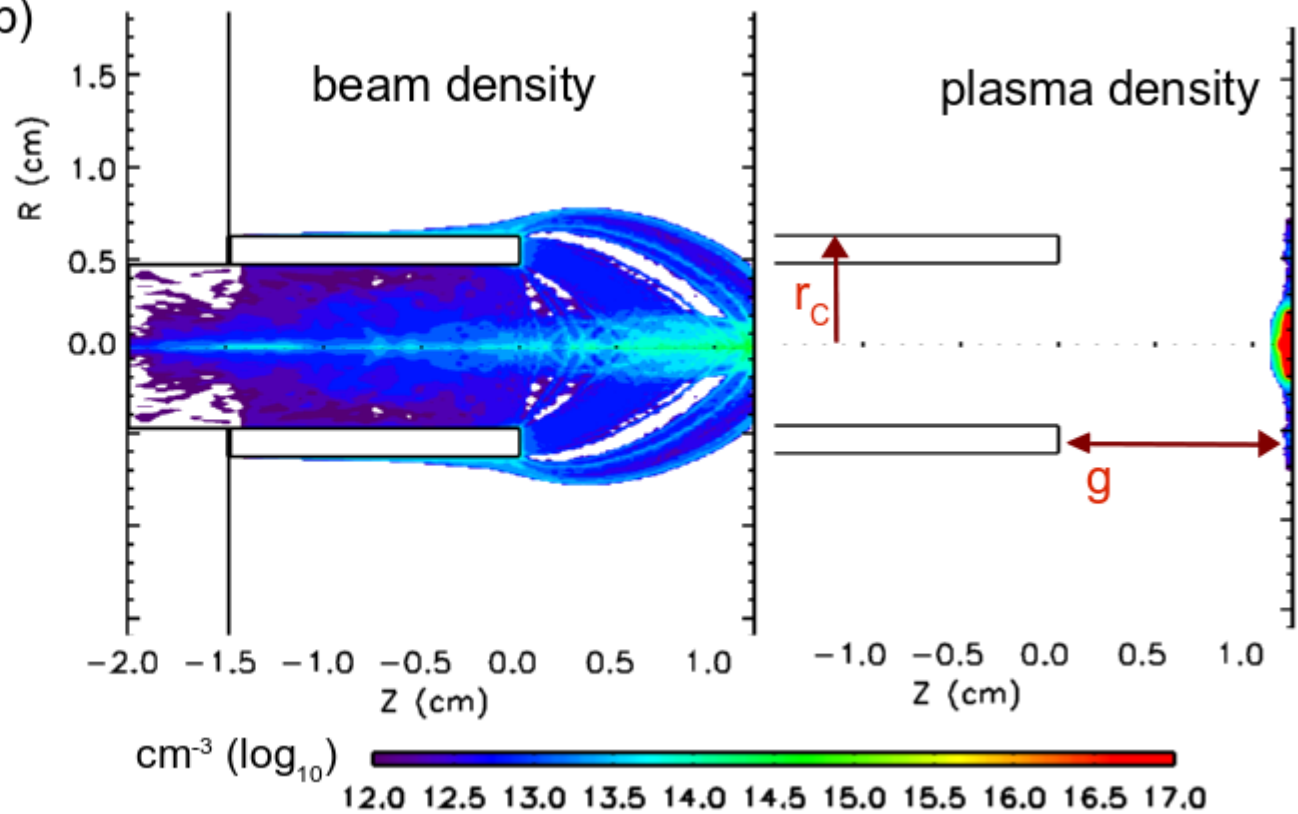


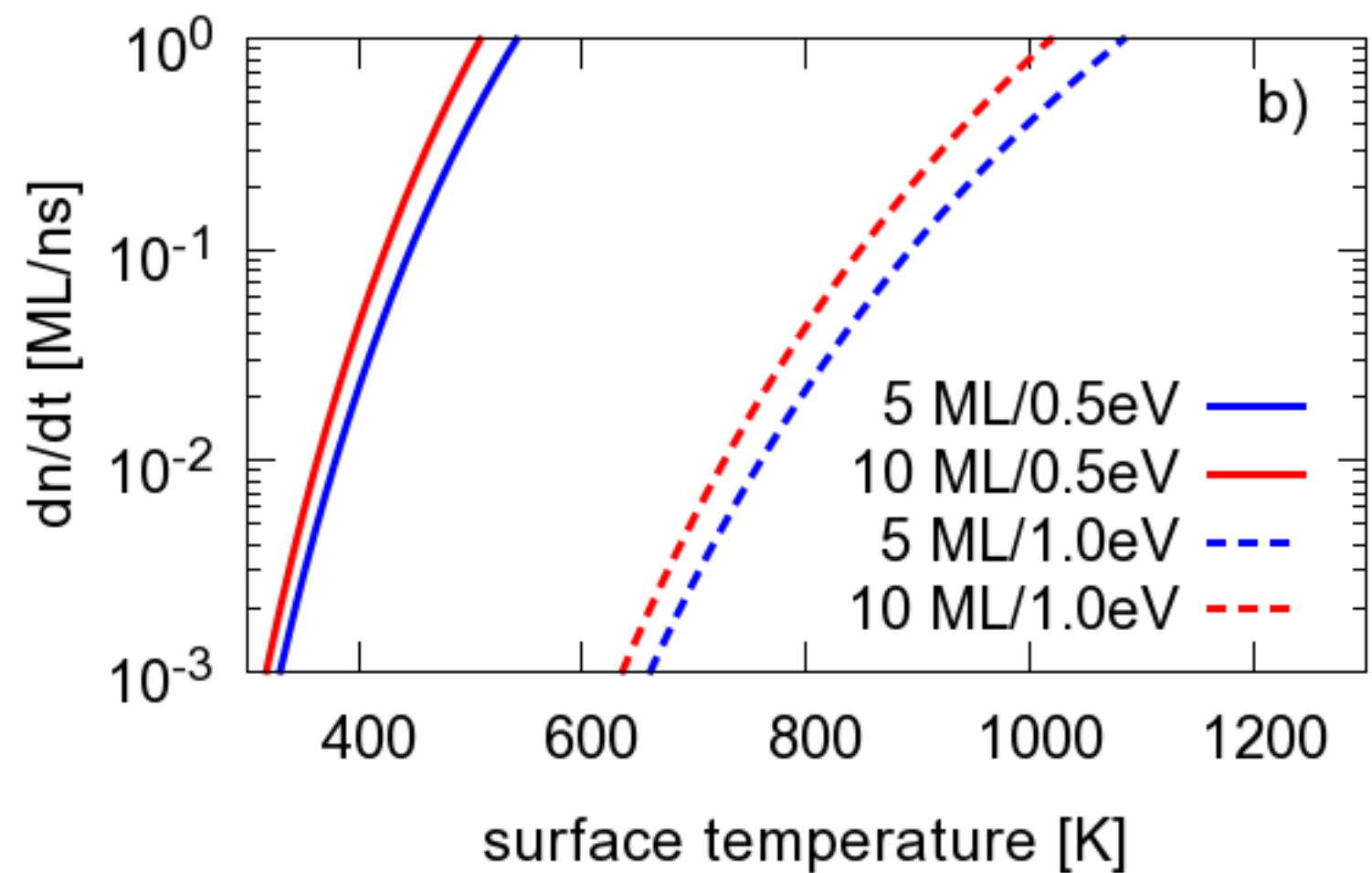
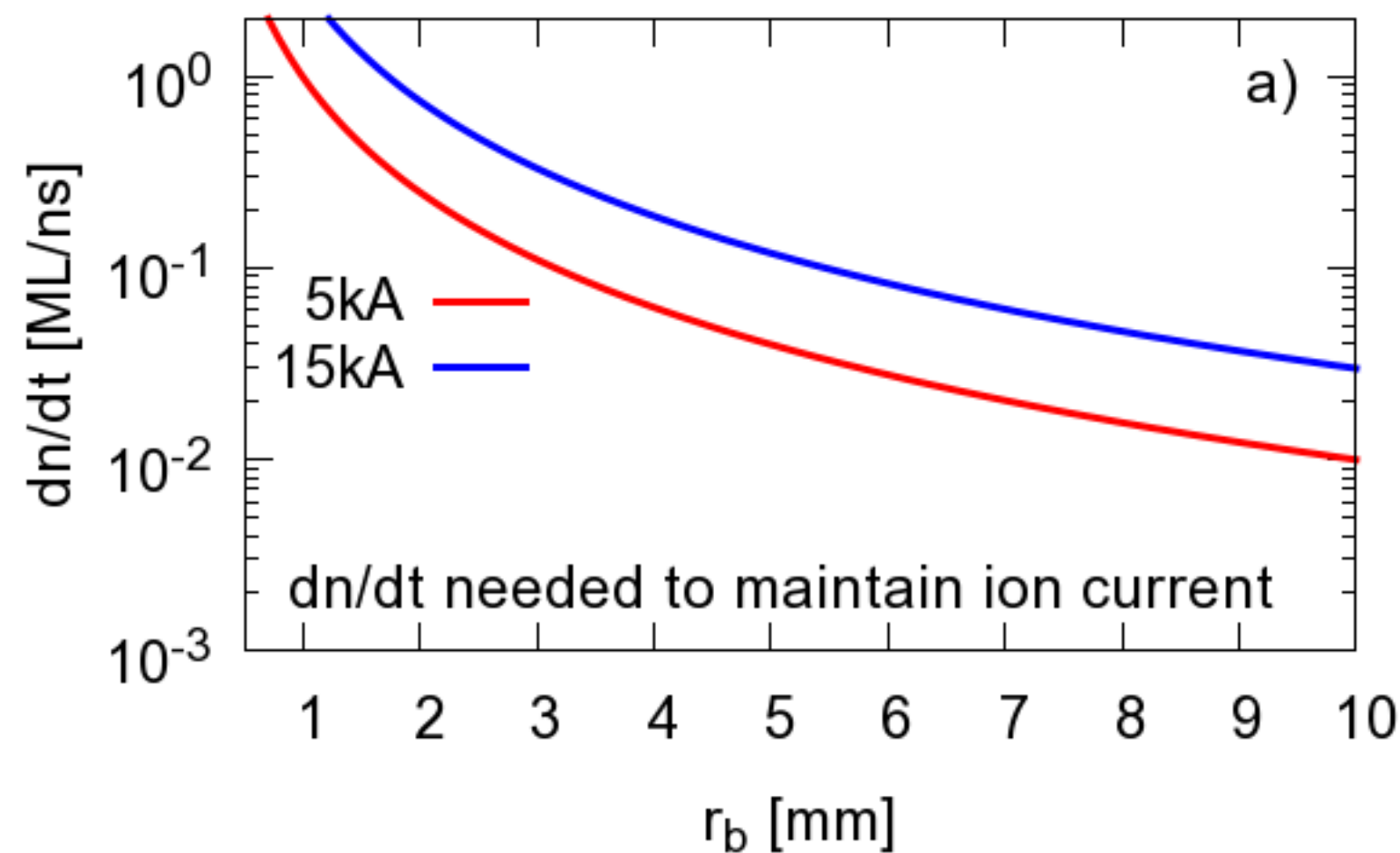


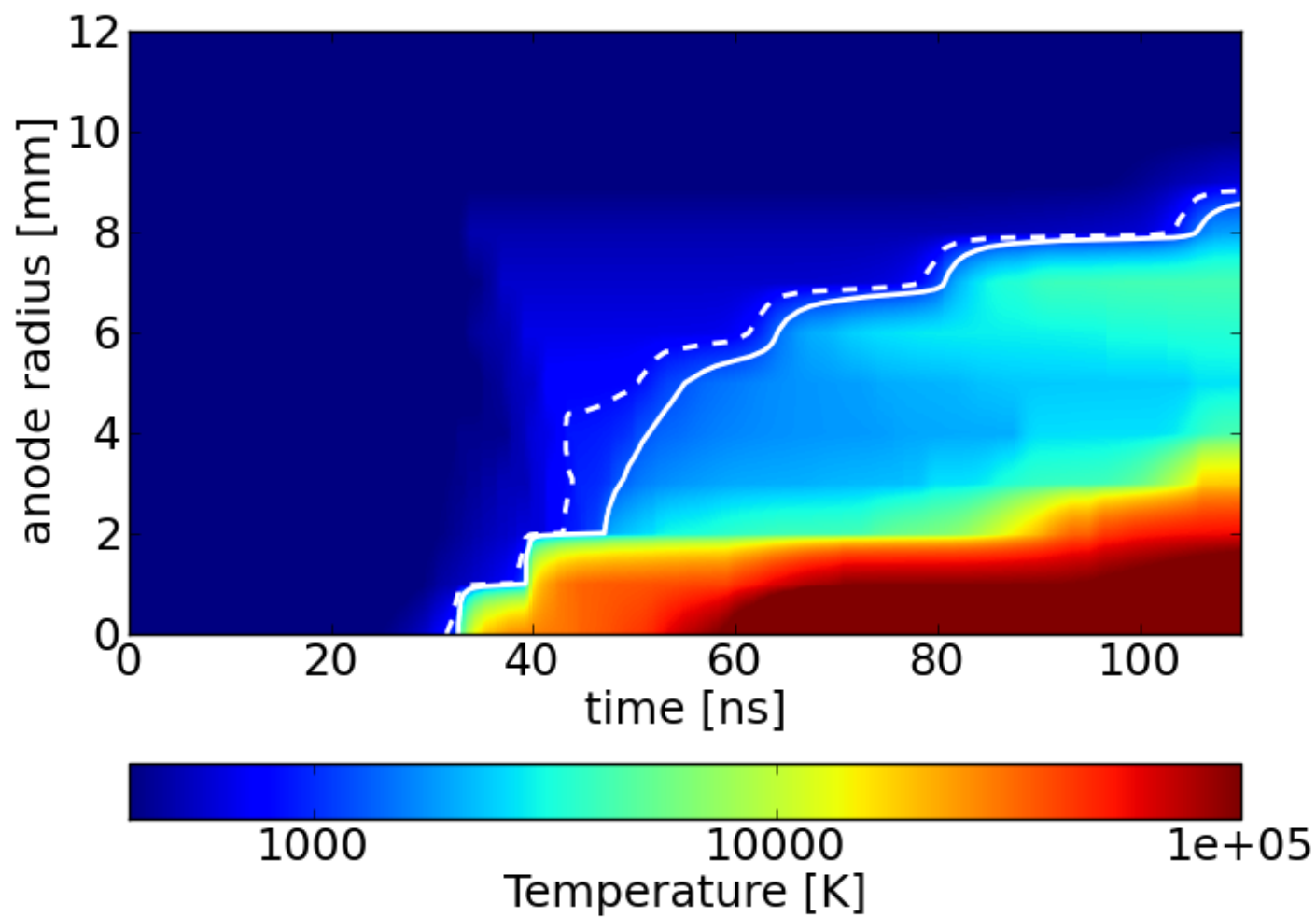
a)



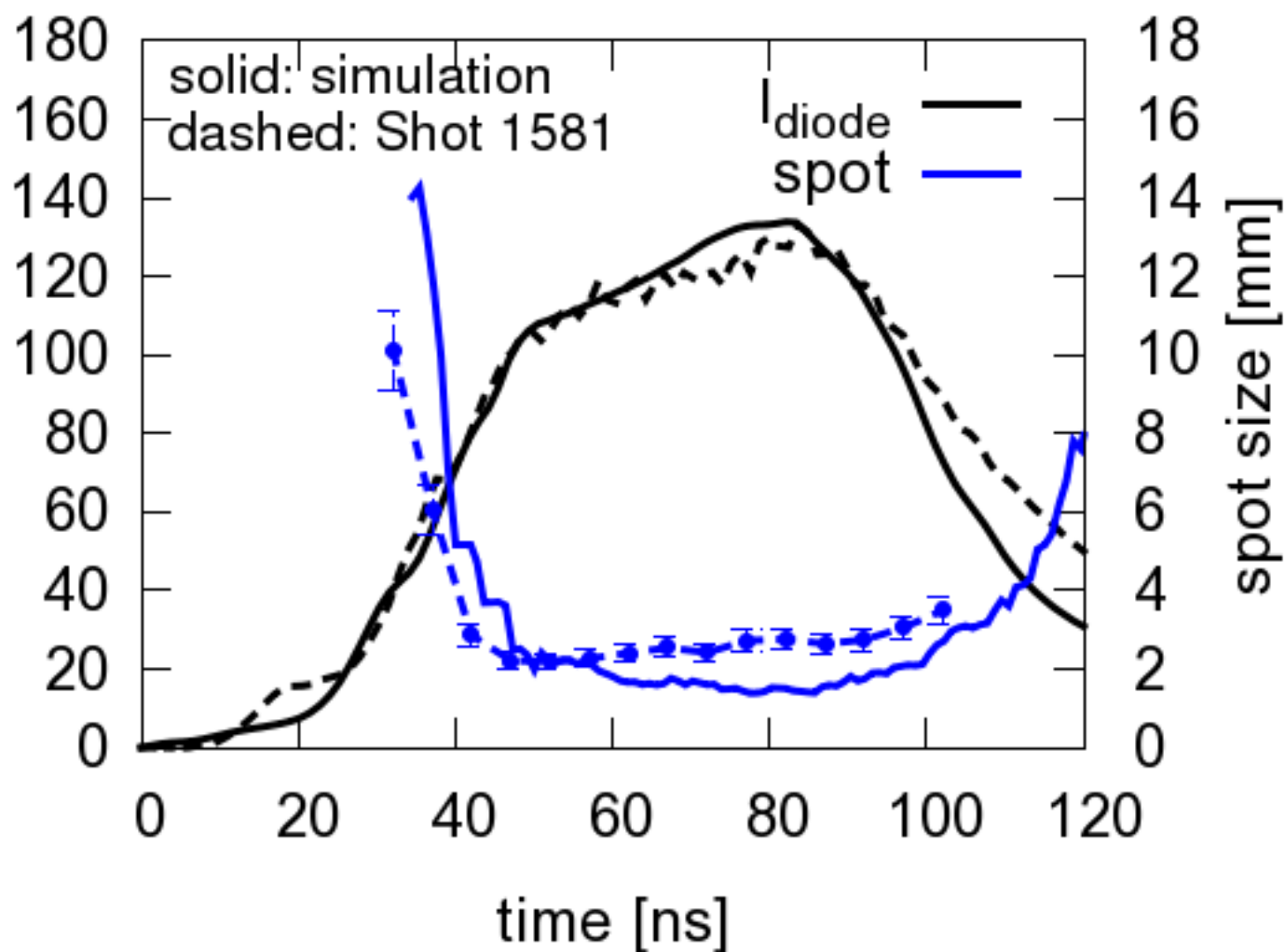
b)

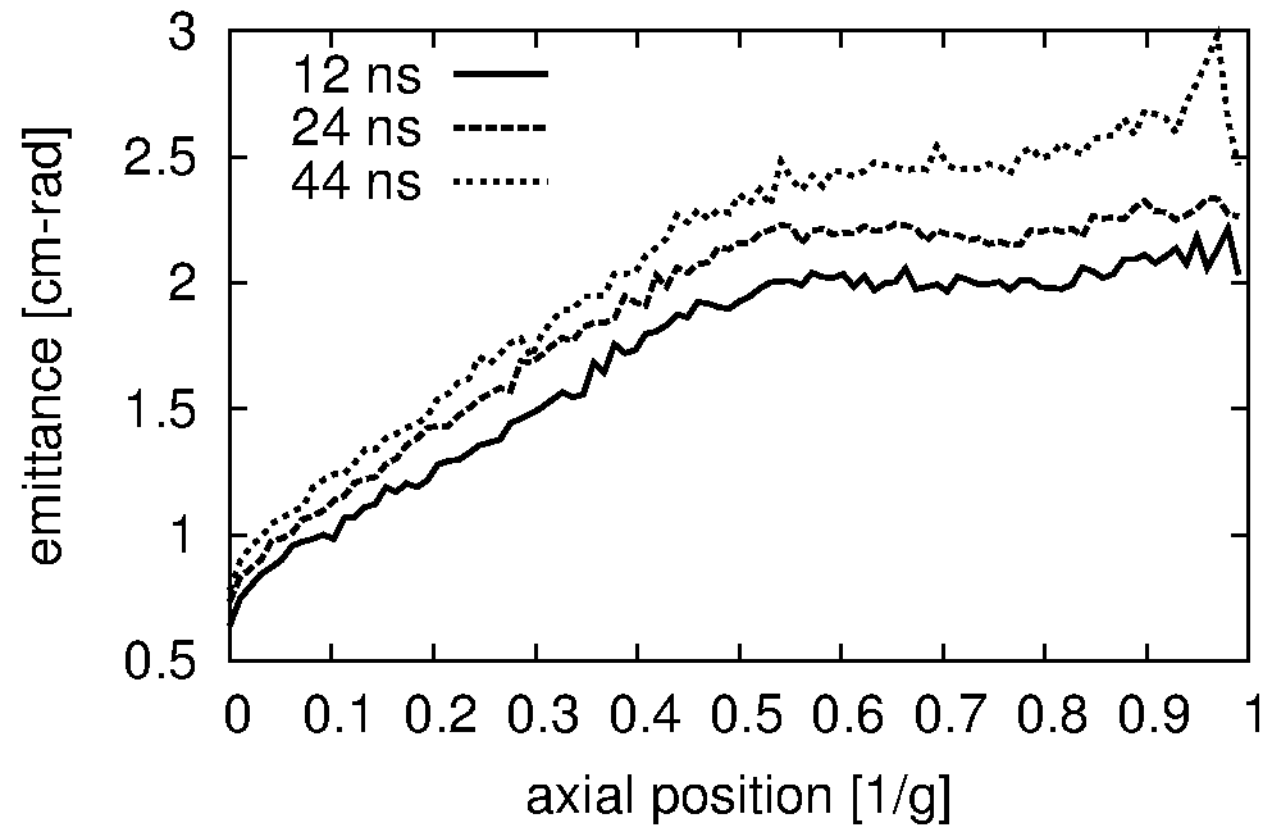


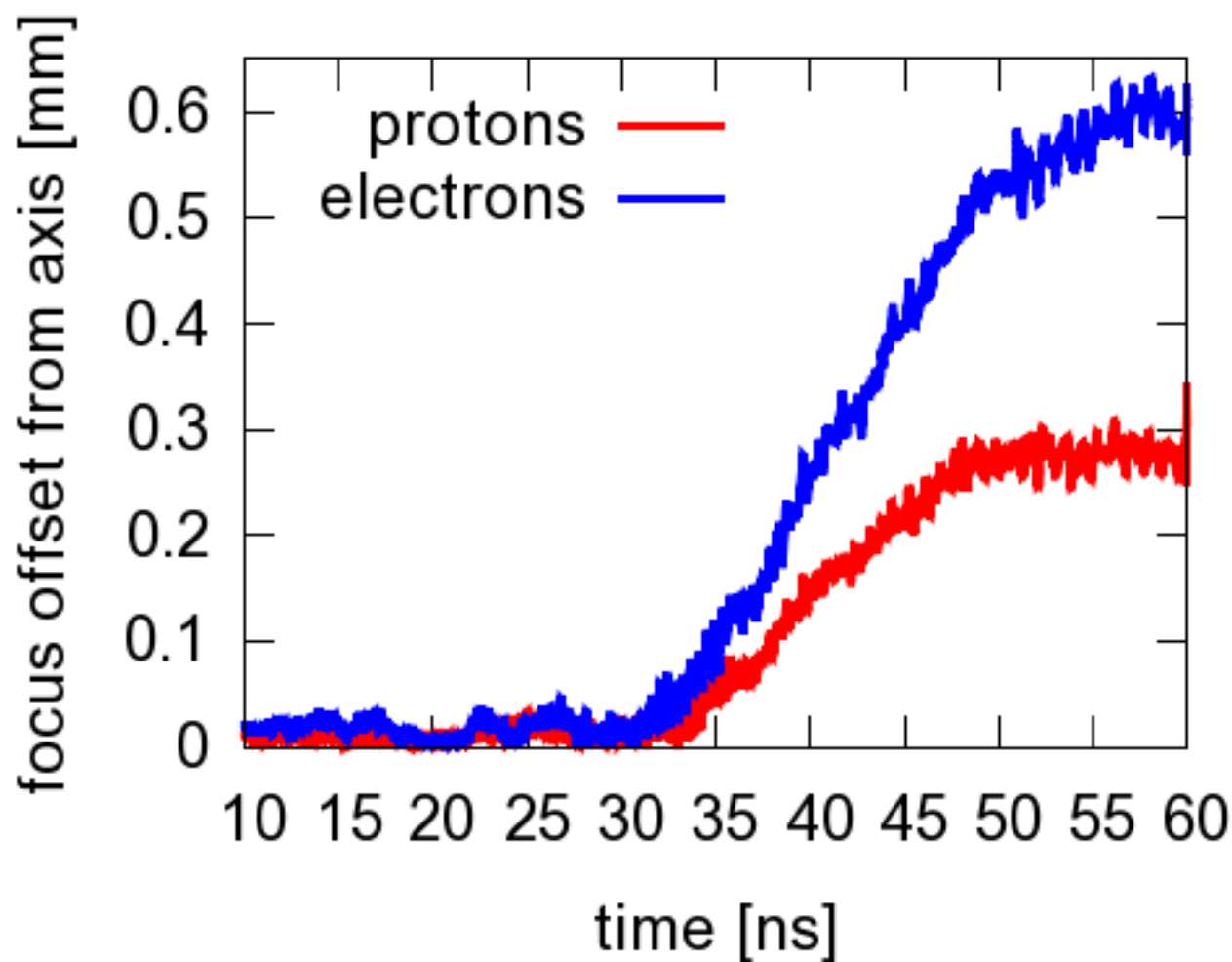


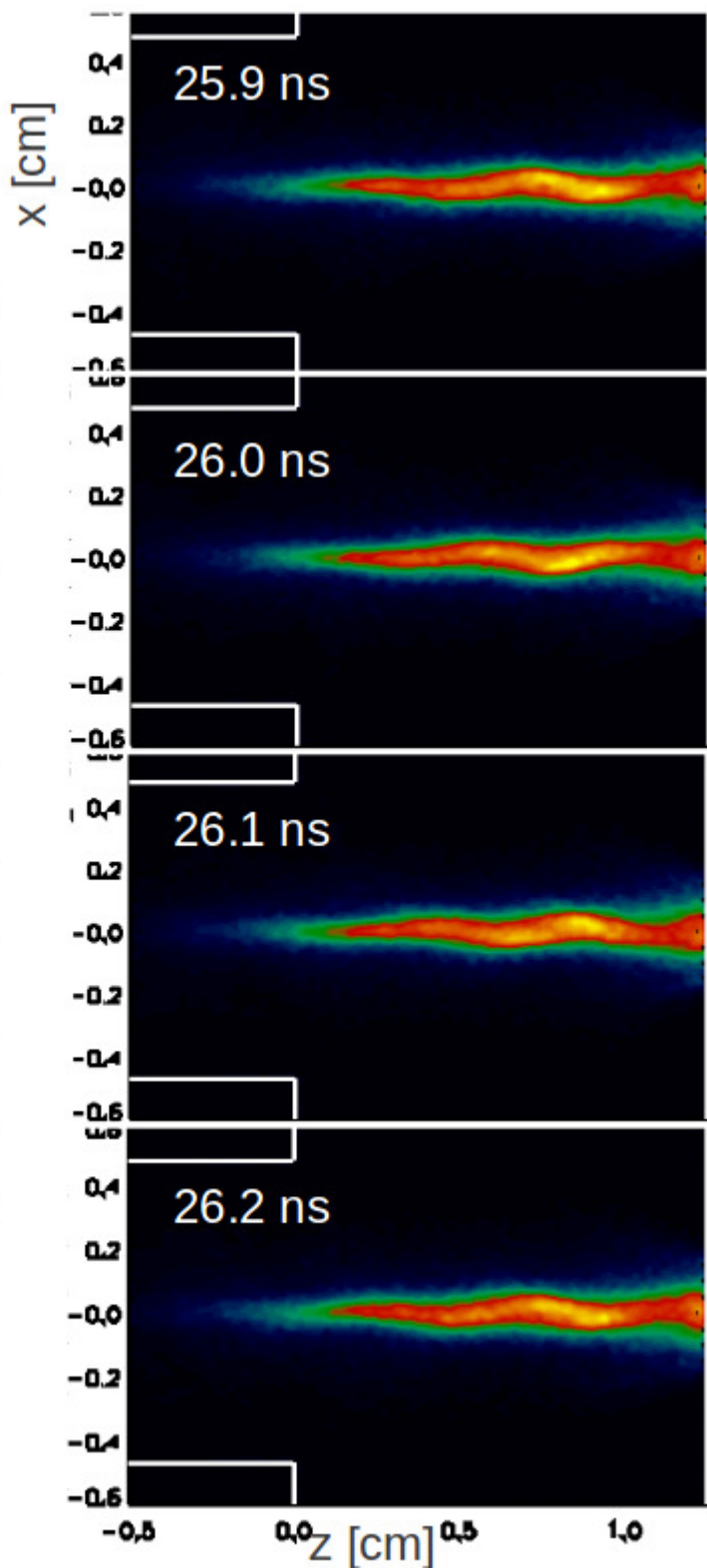
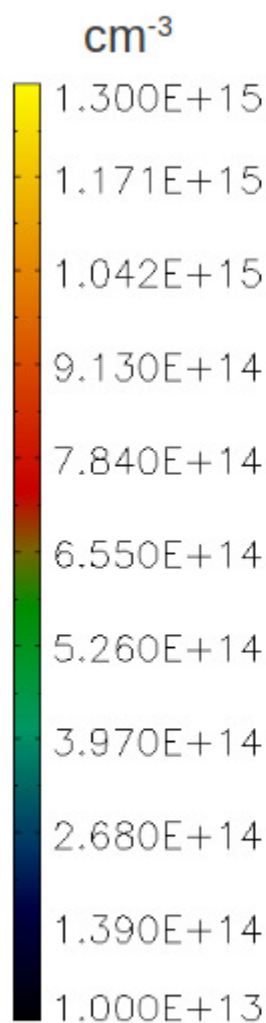


current [kA]









current [kA]

